SAE INTERNATIONAL

ARTICLE INFO
Article ID: 04-15-02-0007

doi:10.4271/04-15-02-0007

Rate Shape Design for Gasoline-Like Fuels at High Injection Pressures Using One-Dimensional Hydraulic Models

Tommy Tzanetakis,[1] Atharva T. Desai,[2] Alexander K. Voice,[1] and Jeffrey D. Naber[2]

[1]Aramco Americas: Aramco Research Center-Detroit, USA
[2]Michigan Technological University, USA

Abstract

Recent research has demonstrated that gasoline compression ignition (GCI) can improve the soot-oxides of nitrogen (NOx) trade-off of conventional diesel engines due to the beneficial properties of light distillate fuels. In addition to air handling and aftertreatment, fuel systems also require further development to realize the potential efficiency and emissions benefits of GCI. Injector one-dimensional (1-D) hydraulic modeling is an important design tool used for this purpose. The current study is a continuation of prior work that used computed physical fuel properties and hydraulic models to accurately simulate high-pressure injection behavior relevant to GCI. With respect to fuel characteristics for the model, physical properties were validated by direct comparison to measurements at temperatures and pressures reaching 150°C and 2500 bar, respectively. Calibration of the injector model discharge coefficients for gasoline-like fuel was automated with various multi-objective optimization approaches coupled to a genetic search algorithm. However, Pareto optimization showed the best closure with an experimental rate of injection (ROI) and total injected quantity compared to other current and previous manual methods. The validated model was then used to determine the injector specifications needed to approach an idealized, slowly opening rate shape that could enable low-NOx combustion. Initial parametric studies of key parameters affecting rate shape showed that changing a combination of nozzle exit, control chamber (or servo) outlet, and needle orifice diameters could produce the desired single injection fueling profile. A transient targeting (TT) optimization technique coupled to a genetic search algorithm was compared to a full-factorial design of experiments (DoE) and showed that both approaches could reasonably achieve the target rate shape. However, TT required a significantly reduced computational runtime. In general, this study provides a robust methodology for accurately simulating gasoline-like fuels in high-pressure injectors and demonstrates a conceptual rate shape targeting process for GCI using 1-D hydraulic models. This tool could potentially be integrated with predictive computational fluid dynamics (CFD) models to achieve a simulation-led combustion system design process that includes rate shaping as an additional avenue for optimization.

History

Received: 21 Sep 2021
Revised: 17 Nov 2021
Accepted: 29 Dec 2021
e-Available: 13 Jan 2022

Keywords

Gasoline compression ignition (GCI), Light distillate fuels, One-dimensional (1-D) hydraulic modeling, High-pressure direct-injection, Multi-objective optimization, Rate shaping, Fuel injection system simulation

Citation

Tzanetakis, T., Desai, A., Voice, A. and Naber, J., "Rate Shape Design for Gasoline-Like Fuels at High Injection Pressures Using One-Dimensional Hydraulic Models," *SAE Int. J. Fuels Lubr.* 15(2):137–170, 2022, doi:10.4271/04-15-02-0007.

ISSN: 1946-3952
e-ISSN: 1946-3960



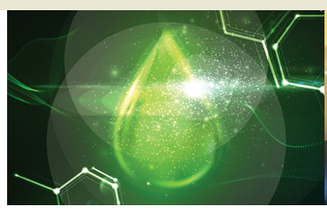

1. Introduction

Liquid petroleum fuels are projected to remain an important part of the transportation energy mix during the next several decades [1, 2]. Their energy density and existing distribution infrastructure have made them a key contributor to global economic growth over the last century and will continue to sustain the increasing demand for energy in the future. However, stringent regulations are currently being introduced to help drive more efficient mobility solutions and balance the benefits of economic growth with known environmental impacts. Ultimately, the regulations are intended to substantially reduce greenhouse gas and criteria pollutant emissions in various energy sectors, including transportation. With these trends in mind, further improvements to liquid petroleum-fueled internal combustion engines are necessary.

Gasoline compression ignition (GCI) has recently been demonstrated as a key enabling technology that can simultaneously increase efficiency and reduce the pollutant emissions of internal combustion engines. Research in heavy-duty commercial transport applications has shown that by controlling injection strategy and leveraging the longer ignition delay, lower viscosity, and higher volatility of gasoline-like fuels to promote mixing, GCI can achieve reduced soot emissions at a relatively low engine-out oxides of nitrogen (NOx) level [3, 4, 5, 6, 7]. The improved soot-NOx trade-off can help mitigate some of the operational and durability demands placed on complex aftertreatment systems intended to meet future ultralow-NOx regulations [5, 8]. However, fully realizing the fuel economy potential of GCI compared to the extremely efficient conventional diesel powertrains will require a system-level optimization approach. This means designing the combustion, air handling, and aftertreatment systems together with a set of efficiency and emissions targets in mind.

Fuel systems are also considered an important technology module for meeting future regulations [9]. Prior studies have shown that very high diesel-like injection pressures may not be necessary for certain partially premixed GCI combustion strategies [10, 11, 12, 13]. However, more recent work has highlighted that fuel pressures in excess of 1000 bar support mixing-controlled GCI and allow for high load operation while simultaneously managing heat release rate and soot emissions [6, 14]. Since current gasoline direct injection hardware does not typically exceed the operating pressures of 700 bar [15], high-pressure diesel architectures should be considered as a starting point. However, redesigning or optimizing the injection equipment for operation with different fuels is not a trivial task and requires the correct tools and techniques.

One-dimensional (1-D) hydraulic models are one such tool widely used throughout industry and research. They can calculate the pressure wave and flow dynamics of a fluid as it interacts with various components in a hardware system. This makes them perfectly suited for assessing the impacts of different fuels on injector performance and estimating leakage flows to properly resize drain orifices or clearance gaps within the system [16, 17, 18, 19, 20, 21]. These types of evaluations are particularly important for high-pressure GCI applications, which require consideration of increased parasitic losses due to the low viscosity of gasoline-like fuels compared to diesel [22]. Coupling 1-D hydraulic models to predictive combustion or engine simulation tools also offers a pathway to determine unique fueling rate profiles (i.e., injection rate shapes) that can further improve efficiency and emissions benefits when optimized together with piston-bowl geometry, injector spray angle, and total hydraulic flow rate [9, 23, 24, 25].

Figure 1 shows that control of the fueling rate profile during combustion, or "rate shaping," can be achieved through various means. Digital rate shaping uses a series of discrete, closely coupled injection events to approach a desired heat release profile [24, 25]. Continuous rate shaping typically employs pressure modulation or direct needle lift control during a single injection event [26, 27]. Continuous techniques

FIGURE 1 Rate shaping categories and techniques.

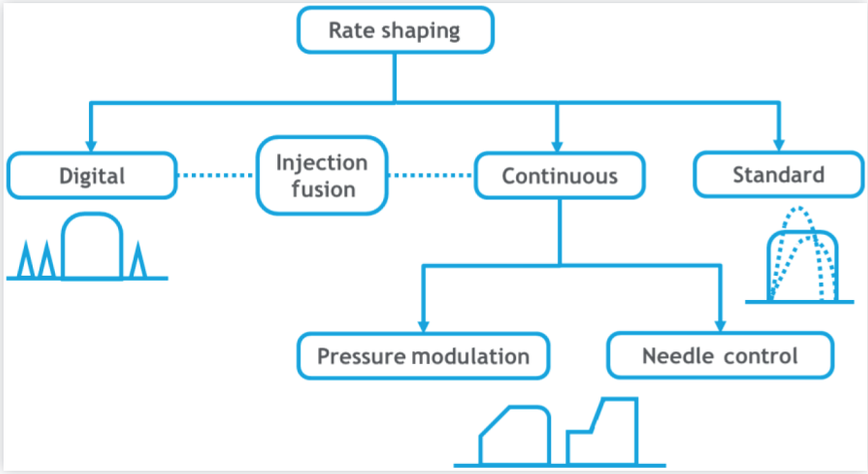

require more specialized hardware such as oil-intensified unit injectors [28, 29], direct-acting piezo injectors [30, 31], switching valves between two separate fuel supply rails [32, 33], and injectors with variable nozzle orifice areas [34, 35] or that have relatively complex internal pilot valve layouts [27, 36]. "Injection fusion" is an alternative approach that bridges the gap between digital and continuous rate shaping [37, 38, 39]. It relies on overlapping the hydraulic pulses from extremely close-coupled injection events to create unique, repeatable fueling profiles within certain dwell time limits. Although fully flexible rate shaping offers an opportunity to design heat release profiles for a specific combustion strategy using closed-loop control [26], there are several cost, complexity, and durability concerns associated with practical implementation. A degree of rate shaping, however, can still be achieved using standard solenoid injectors by adjusting their internal hydraulic dimensions [40].

A summary of different rate shapes used in compression ignition applications is provided in Figure 2 [41]. Pilot injections, slow main opening ramps, and "boot"-shaped profiles spread out initial heat release leading to lower peak cylinder temperature, reduced NOx emissions, and quieter combustion [30, 33, 36, 42, 43]. Pilot injections can also reduce noise through the mechanism of destructive pressure wave interference from the heat release of separate fuel pulses [44]. Closely coupled post injections enhance turbulent mixing and secondary heat release after the main combustion event [45, 46]. This promotes later stage soot oxidation and can reduce exhaust particulate emissions [47]. Very late post injections are used for managing exhaust gas temperatures during aftertreatment system warm-up or regeneration and are not considered a combustion rate shaping technique. Fast main closing ramps can lead to air entrainment rates two to three times higher than those of a steady free jet [48]. This "entrainment wave" enhances near-nozzle air availability that can promote soot oxidation, but also quench the burnout of hydrocarbons due to overleaning. Post injections are also effective at reducing unburned hydrocarbon (UHC) emissions because they enrich this region with fuel and cause secondary heat release [49]. Finally, main closing ramps can be used to control the onset of "combustion recession," which occurs when the spray flame propagates from its quasi-steady lift-off length back towards the nozzle tip at the end of injection [50, 51]. Although a slow closing ramp reduces the entrainment wave strength, it can promote combustion recession and the burnout of near-nozzle soot and UHCs [51, 52].

It is evident from this brief survey that injection rate shaping can play a significant role in controlling emissions. However, a balance must be struck with fuel efficiency tradeoffs that have been observed when employing this approach. For example, rate shapes that spread out heat release can also degrade fuel consumption because of prolonged combustion duration. This is true for both digital and continuous techniques such as post injection and slow main opening ramps [36, 47, 53, 54]. In addition, the wide range of fueling profiles that can be generated using different hardware configurations and the complex relationship they have with combustion phenomena such as entrainment waves, recession, and secondary heat release suggest that a practical rate shape design should be carried out with tools that consider all these factors simultaneously. Previous work has demonstrated this by using design of experiments (DoE)-based engine testing campaigns [27] and 1-D hydraulic models coupled to predictive combustion simulation tools [24, 25]. Therefore, developing high-pressure injector models for gasoline-like fuels is a means of enabling this path for GCI.

In addition to defining the electrical and mechanical components of a system, 1-D hydraulic models require accurate physical fuel properties. These include density, viscosity, heat capacity, thermal conductivity, saturation pressure, etc. Current 1-D software packages have data for diesel up to injection pressures of 3000 bar [55]. However, the same is not true for gasoline-like fuels which typically only reach pressures of 500 bar in their applications. Light distillate properties will be needed at higher injection pressures to further investigate rate shaping for GCI. Direct measurement of the properties has been reported for middle distillates but requires special equipment that may not be readily available [56, 57]. Another option for multicomponent fuels is to formulate a reduced surrogate and calculate the representative

FIGURE 2 Summary of rate shapes used to control combustion performance and emissions.

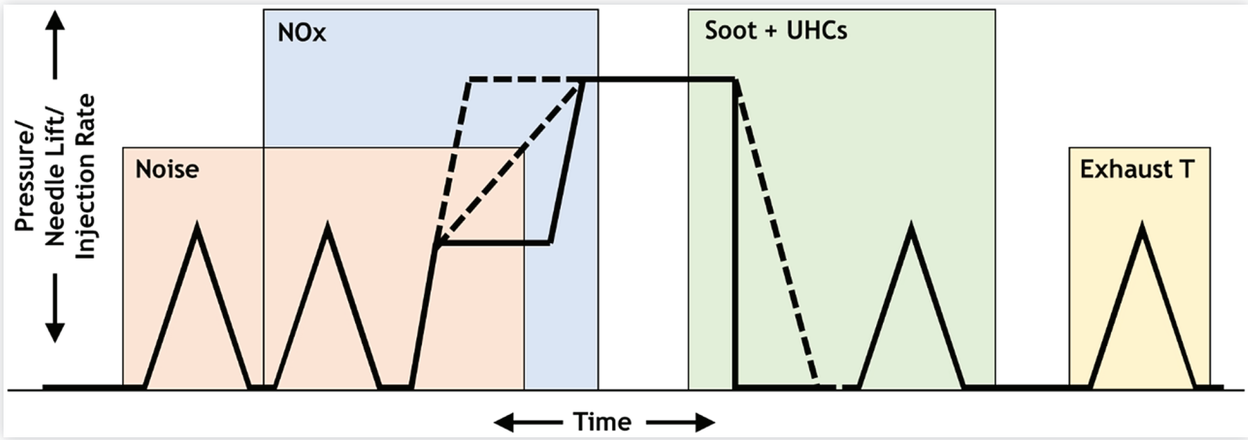

mixture properties. Numerous strategies exist for doing this, which attempt to match physical and chemic kinetic properties simultaneously [58]. Although extremely effective at simplifying the complexity of real fuels for subsequent modeling activities, this approach can potentially compromise the accuracy of properties by using a constrained species palette.

This study is a continuation of previous work that presented a novel methodology for generating accurate liquid property databases of real multicomponent, gasoline-like fuels [59]. The method uses a "bottom-up" surrogate formulation approach that matches the entire measured listing of chemical species in the fuel as closely as possible. This ensures that subsequent property calculations maintain inherently better accuracy over any reduced surrogate formulation approach. The new method is perfectly suited to 1-D hydraulic models, which only require tabulated physical properties and resolves situations where light distillate data does not exist or cannot be readily measured for the temperature-pressure range of interest.

In the current work, this new property calculation method was used to adapt an existing 1-D hydraulic diesel injector model and accurately simulate gasoline-like fuel behavior at high pressures. The calculated gasoline fuel properties were validated by direct comparison to measurements at temperatures and pressures reaching 150°C and 2500 bar, respectively. Calibration was performed against experimental gasoline injection rate data using objective function minimization techniques coupled to a genetic search algorithm. The fully validated 1-D model was then used to demonstrate a targeting process for conceptual GCI rate shape profiles by adjusting internal hydraulic parameters.

2. Materials and Methods

2.1. Test Fuels

Standard test fuel properties are reported in Table 1. The United States (U.S.) market gasoline containing 10% ethanol by volume (E10) was not used directly but presented as a reference. The diesel was a European Standard (EN) 590 European formulation containing fatty acid methyl esters (FAME) which contributed to a relatively high cetane number and low wear scar diameter (WSD) [60, 61, 62]. The light distillate fuel is termed "RON60" because it had a research octane number (RON) of only 56.6. Although the octane rating and chemical composition of RON60 were different from market gasoline, the fuels shared similar physical properties including density, viscosity, distillation, and vapor pressure. This makes RON60 a viable candidate for studying the general hydraulic characteristics of gasoline-like fuels and establishing modeling practices that can be applied to other light distillates, such as E10.

TABLE 1 Fuel properties of RON60 gasoline compared to typical diesel and market gasoline.

Property	Units	Diesel	RON60 gasoline	E10 market gasoline
Density(1)	kg/m^3	838	714	744
Viscosity(2)	mm^2/s	4.00	0.593	0.629
IBP(3)	°C	182	40.0	36.7
T10	°C	210	72.0	54.3
T50	°C	273	98.5	92.1
T90	°C	337	124	158
FBP	°C	361	134	197
RVP(4)	kPa	<7	38.8	63.5
WSD(5)	µm	172	240	770
Aromatics(6)	wt%	26.4	7.2	20.9
Oxygen(7)	wt%	0.65	<0.05	3.67
Sulfur(8)	mg/kg	5.2	16.5	9.9
H/C ratio(9)	mol/mol	1.84	2.15	1.99
LHV(10)	MJ/kg	42.7	44.0	41.8
Cetane number(11)	—	51.3	34.4	19.9
RON(12)	—	—	56.6	91.8

Notes: (1) Diesel at 15°C using the International Organization for standardization standard (ISO) 12185 and gasoline at 15.56°C using the American Society for testing and Materials standard (ASTM) D4052; (2) All viscosities reported at 20°C using ISO 3104 for diesel and ASTM D445 for gasoline; (3) Distillation curves measured using ISO 3405 for diesel and ASTM D86 for gasoline; (4) Vapor pressure of diesel was below detection limit of 6.98 kPa for the ASTM D5191 gasoline method; (5) WSD as per high frequency reciprocating rig method at 60°C for diesel using ISO 12156-1 and 25°C for gasoline using ASTM D6079; (6) ISO 12916 for diesel and ASTM D1319 for gasoline; (7) Due to the presence of FAME in diesel fuel as measured by EN 14078, using ASTM D5622 for direct oxygen determination; (8) ISO 20884 for diesel and ASTM D5453 for gasoline; (9) Calculated from results of ASTM D5291; (10) Lower heating value as determined via ASTM D240; (11) ISO 5165 for diesel and ASTM D6890 for derived cetane number of gasoline as determined by the ignition quality tester method; (12) ASTM methods D2699 and D2700 for gasoline only

As evidenced by market gasoline data in Table 1, the WSD of neat light distillates typically falls between 700-1000 µm when measured at 25°C [63]. This exceeds the recommended maximum value of 380 µm intended to protect high-pressure injection systems from fuels with poor lubricity [64]. Based on the results of a prior evaluation study, RON60 was dosed with 200 ppm of lubricity-improving additive to bring its WSD within acceptable limits [65].

2.2. Injector

Figure 3 shows the heavy-duty Cummins production injector investigated in this work [59]. Considering on-road commercial transport applications, this hardware is used in 15 L Class 8 truck engines and rated for fuel pressures up to 2500 bar. The eight-hole nozzle tip geometry is that of a typical high-pressure common rail diesel injector and has been previously characterized with high-resolution X-ray computed tomography scans [66].

A schematic of the internal configuration is also shown in Figure 3. It consists of a solenoid actuated two-way pilot valve and a hydraulically lifted main needle. During injection, the solenoid is powered on to open the pilot valve and throttle high-pressure fuel through the control chamber inlet orifice. This creates lower pressure in the control chamber and a resultant force imbalance on the main needle (or plunger) which lifts it off its seat. High-pressure fuel is supplied to the nozzle sac and spray holes via upstream needle orifice(s). Fuel passing through the control chamber outlet orifice and pilot valve is eventually drained to the low-pressure return system as dynamic leakage. To stop the injection, the solenoid is powered off, which closes the pilot valve and allows the control chamber to refill with high-pressure fuel. Along with the aid of a return spring, this process forces the main needle to re-seat and terminate flow through the spray holes.

The heavy-duty Cummins injector architecture does not support fully flexible, on-demand rate shaping. However, various hydraulic elements can be adjusted to permanently shift the fueling profile. Increasing the nozzle hole exit area helps to increase the peak flow rate at a given injection pressure [9]. Adjusting the nozzle hole K-factor (i.e., taper), inlet radius of curvature, nozzle sac type or volume, and main needle seat geometry can also influence the overall rate shape [29, 67, 68, 69]. Finally, the fueling rate is very sensitive to control chamber volume and orifice geometry [17, 40]. For example, the rate of chamber fluid volume change (Q_{inlet}) is directly proportional to the inlet orifice diameter and determines the main needle closing velocity (v_{close}) once the pilot valve is shut. Figure 3 summarizes the potential levels of rate shape adjustment for

FIGURE 3 Schematic of 2500 bar heavy-duty Cummins production injector showing different hardware levels that impact the rate shape.

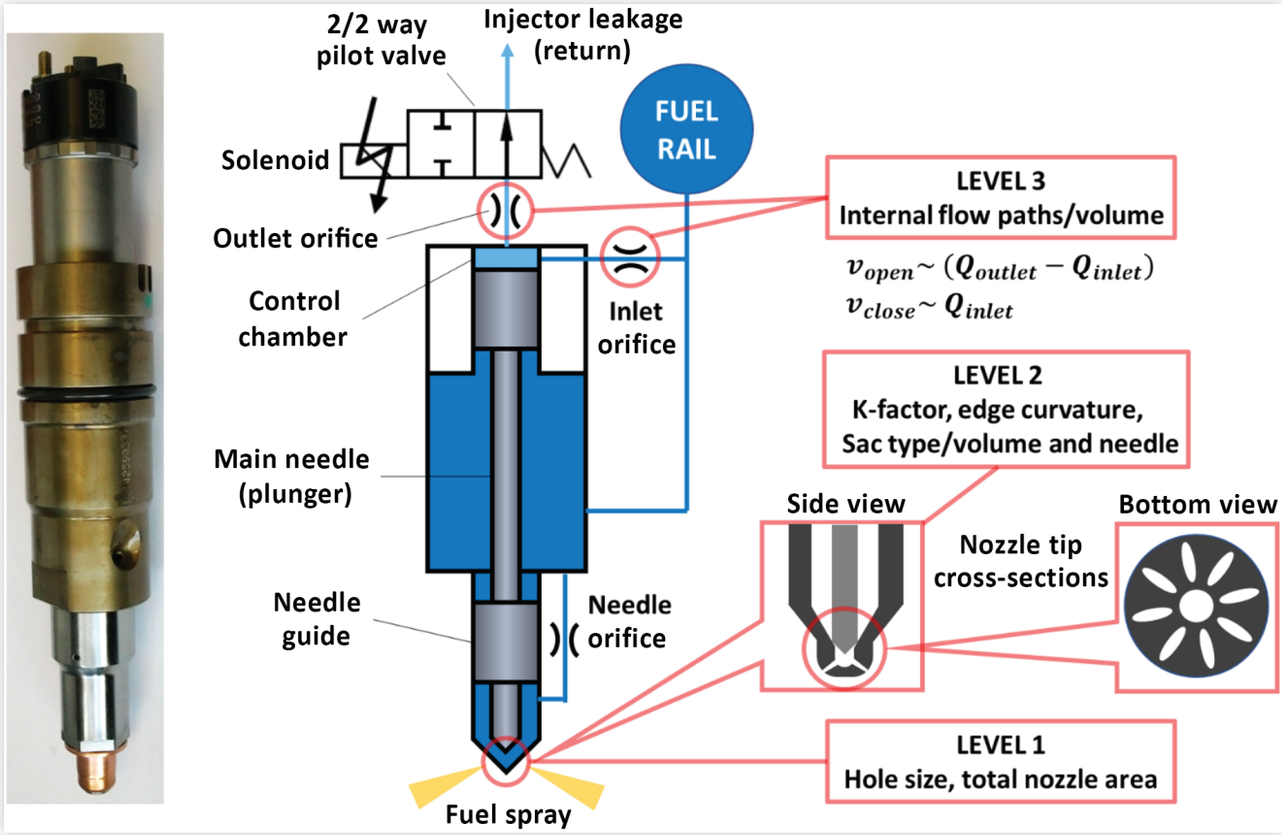

a standard solenoid injector. The impact that most of these parameters have on rate shape can be assessed using a 1-D hydraulic model. They may also be considered in combination to target unique fueling profiles. Electrical parameters such as hold current and boost voltage do not significantly influence the rate shape of diesel injections and were thus not considered further [40].

2.3. Fuel System Setup

Figure 4 shows a schematic of the fuel system test bench used to acquire experimental rate of injection (ROI) data. The details of this configuration have been previously discussed in several prior studies [22, 59]. It contained all the fuel system components as they appear on a model year 2014 Cummins ISX15 engine including the inlet metering valve (IMV), high-pressure pump (HPP), rail pressure sensor (RPS), and (high) pressure relief valve (HPV). The system was driven by an electric motor (M) coupled to the HPP via a torque flange (T). Actuation and feedback signals for the injectors, IMV, and RPS were achieved using a flexible control module (FCM), which allowed for independent fueling quantity, pump speed, and rail pressure set points. A full set of six injectors was installed and operated using a common staggered-fire mode as they would be on the engine. This setup ensured that the hydraulic performance of the system emulated real operation on an engine as closely as possible. The only difference was that the injected fuel did not undergo combustion and was simply circulated back to the main supply tank after being cooled. A separate oil supply line was used to provide lubrication to the bottom end of the HPP, which is a typical design feature of heavy-duty pumps.

2.4. Hydraulic Measurements

A commercial injection analyzer (IA) was used to measure the ROI for the Cummins injector. Figure 4 shows that this device was only connected to one of the six injectors on the system at any given time. The analyzer uses the principle of a Bosch rate tube, which relates the amplitude of a hydraulic pressure pulse to the injected mass via the cross-sectional tube area and speed of sound in the fluid [70, 71]. Several forms of data can be extracted from the analyzer including instantaneous ROI profiles, total fuel quantity per injection, curves of the total injected mass versus electronic duration (or "gain curves"), and hydraulic opening/closing delays. Table 2 lists

FIGURE 4 Fuel system setup used for hydraulic injector performance measurements.

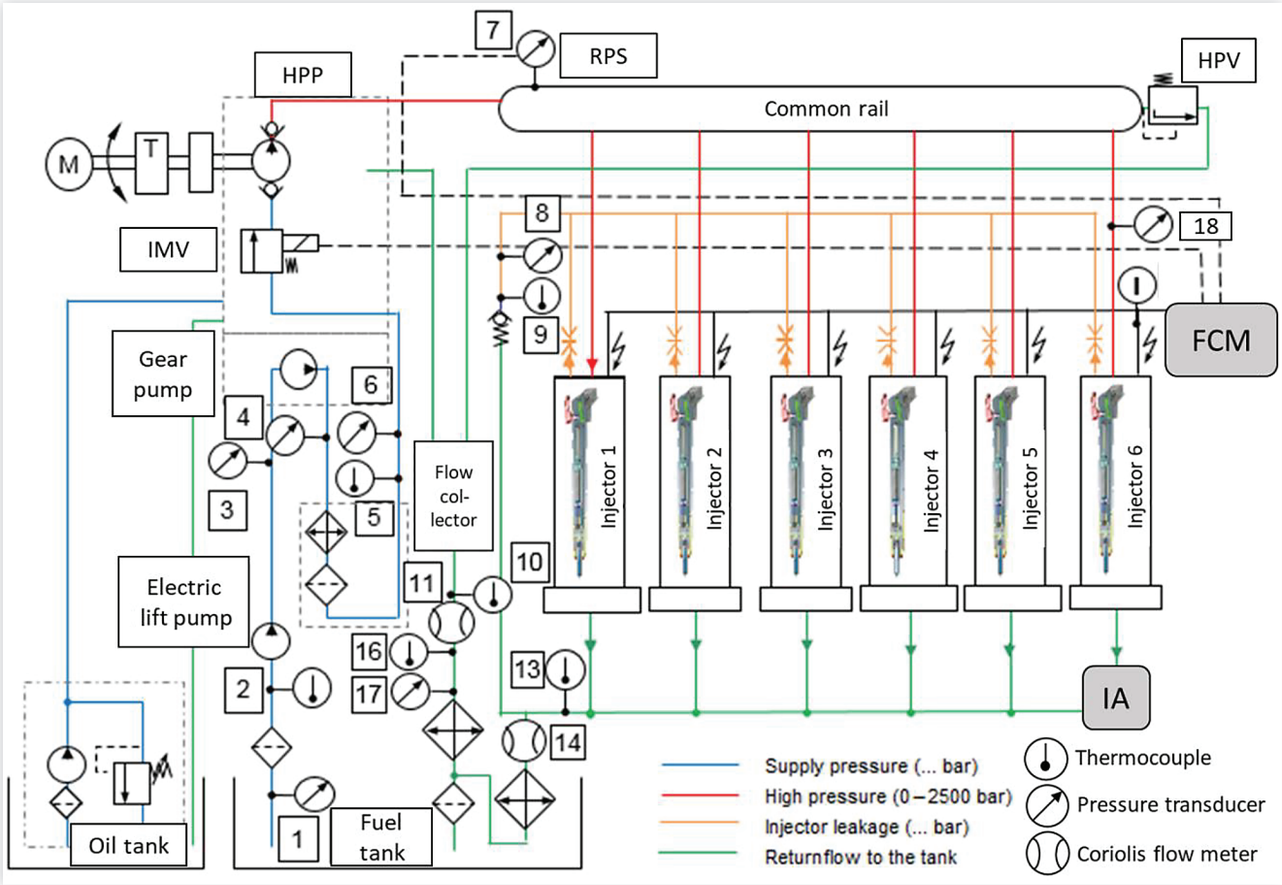

TABLE 2 SET load point specifications for ROI measurements.

Load point	Pump speed (RPM)	Electronic injection duration (ms)		Rail pressure (bar)	
		Diesel	RON60	Diesel	RON60
A75	1147	1.96	1.96	1880	1900
B50	1375	1.42	1.36	1422	1500
C100	1602	1.77	1.82	2500	2500

important supplemental emissions test (SET) load points at which high-fidelity ROI profiles were measured for both diesel and RON60 fuels. Three completely new injectors were analyzed to capture production performance variability in the results. This was done by swapping out "Injector 6" with fresh injectors when the measurements were performed. Reported experimental ROI profiles are an average of 500 individual injection events. For gain curve measurements, the pump speed was set to 1500 revolutions per minute (RPM) while electronic duration and rail pressure were varied across the entire operating range of the injector (i.e., up to 2.75 ms and 2500 bar, respectively). The backpressure for all hydraulic measurements was set to 50 bar.

2.5. 1-D Hydraulic Model

A 1-D hydraulic model of the Cummins injector was developed in GT-SUITE [55]. The typical steps in this process have been thoroughly documented in the literature [16, 72, 73], so only a very brief overview will be provided here. The first step is to characterize the hydraulic performance of the injector over its entire operating range. This is accomplished using test bench setups and IA equipment like those previously described. Next, visualization techniques such as X-ray computed tomography are employed to determine the size of internal hydraulic components, passages, and clearances needed for the model. The third step is to disassemble the injector and evaluate the mass of moving bodies, spring constants, and solenoid coil properties. Once all the geometric, mechanical, electrical, and fuel specifications are built into GT-SUITE, the final step is to calibrate the model against measured hydraulic data by appropriately adjusting coefficients. Prior work has shown that a 1-D model of the Cummins injector developed using this process can accurately simulate real diesel fuel system performance [59]. However, updated fuel properties and minor recalibration of the discharge coefficients were needed to reproduce the gasoline hydraulic performance at high injection pressures.

2.6. Surrogate Formulation and Physical Property Generation

The process by which physical properties are generated for light distillates is shown in Figure 5 [59]. After acquiring a real fuel sample, the first step is to determine chemical composition. For petroleum-based fuels, this is typically performed via detailed hydrocarbon analysis (DHA, ASTM D6730); The next step is to formulate a representative surrogate. This is achieved by matching each molecule identified from the DHA with its closest structural equivalent available in a chemical process software or physical property correlation database, such as Aspen HYSYS [74]. At best, a molecule identified in the DHA also exists in the database and is exactly replicated in the surrogate. When an exact match is not possible, the most structurally equivalent chemical surrogate is chosen based on a hierarchical selection process. Continuing in this manner for every species leads to a highly detailed surrogate mixture representing each fuel component as closely as possible. This ensures inherently more accurate properties compared to reduced surrogate formulation approaches; The third step is to generate physical properties over the temperature-pressure range of interest (i.e., 20-225°C and 1-2500 bar, respectively). Chemical database tools do this by employing an equation of state (i.e., Peng-Robinson) along with various built-in correlations or models that can calculate the bulk properties of complex mixtures; The fourth and final step is

FIGURE 5 Process for generating physical fuel properties to use in 1-D hydraulic models.

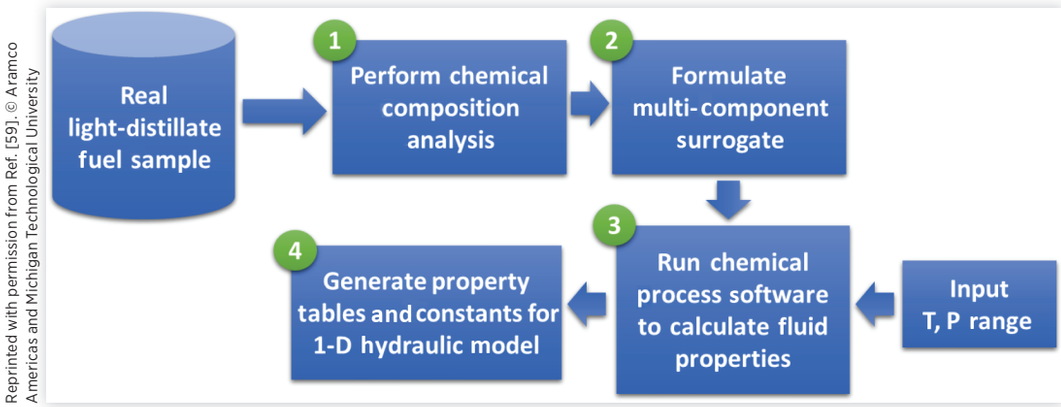

to integrate these fuel properties within the 1-D model. For GT-SUITE, this involves specifying parameters in the "FluidLiqCompressible" and "FluidGas" templates. Additional details pertaining to this patent-pending methodology may be found elsewhere [59, 75].

2.7. Fuel Property Measurements at High Temperature and Pressure

A comparison of the calculated versus measured liquid fuel properties for RON60 gasoline was conducted in a prior work and showed very good agreement [59]. In the current study, validation of the generated properties was extended to temperatures and pressures that represent hydraulic conditions in common rail fuel systems. Table 3 summarizes these conditions along with the properties that were experimentally determined. All measurements were performed using a completely sealed, stainless steel sample container equipped with a metal bellows expansion joint. This allowed the container volume to change along with the liquid at different conditions while maintaining an absolutely zero excess volume or "headspace" for vapor. Furthermore, conditions in Table 3 for which the RON60 fluid model predicted a non-zero-equilibrium vapor fraction were completely avoided to ensure that the measurements were not compromised by phase change. These conditions only presented at atmospheric pressure and temperatures ≥80°C.

A detailed description of all the measurement techniques and their corresponding apparatuses is beyond the scope of this work. Therefore, each method will simply be listed here with references for further reading. Density was measured by accurately determining the weight of fluid and monitoring volume changes through the linear displacement of a sealed piston-cylinder assembly at micrometer (μm) resolution [76]. Dynamic viscosity was measured using a torsional quartz crystal viscometer probe immersed in the sealed sample container [77, 78, 79, 80, 81]. Thermal conductivity was determined using a transient hot-wire probe adhering to the standard test method of ASTM D7896 [82, 83, 84]. Finally, isobaric specific heat capacity was measured using an adiabatic calorimeter as described in the standard test method of ASTM D2766 [85].

TABLE 3 Summary of high pressure and temperature liquid fuel property measurement conditions for RON60 gasoline.

Parameter	Range/technique
Measured properties	Density (ρ_l), viscosity (μ_l), thermal conductivity (k_l), isobaric specific heat capacity ($c_{P,l}$)
Temperature (°C)	−20, 20, 80, 120, 150
Pressure (bar, gauge)	0, 200, 500, 1000, 2500

2.8. Optimization Techniques

A typical design optimization procedure is shown in Figure 6. After simulating a system's performance based on various input parameters and generating its output response, the results are evaluated using an objective function (f). In the case of a 1-D injector model, the input variables could be the nozzle exit hole diameter, servo chamber inlet diameter, etc., while important output responses might be the injection rate shape, hydraulic duration, total injected fuel mass quantity, etc. In many applications, the goal is to find a set of design parameters that minimizes the difference between one or more outputs (R_i) and corresponding target ($R_{i,target}$) responses. The delta between R_i and $R_{i,target}$ forms the objective function to be minimized. When used appropriately, these techniques offer a reduced computational runtime compared to a traditional full-factorial DoE approach.

The Integrated Design Optimizer in GT-SUITE contains a variety of built-in objective function definitions including Multi-Objective Pareto (MOP), Multi-Objective Weighted Sum (MOWS), and Transient Targeting (TT) [86, 87]. In MOP, the objective function for a specific response is given by the following:

$$f_i = \left(R_i - R_{i,target}\right)^2 \qquad \text{Eq. (1)}$$

It is usually not possible to minimize all the objective functions simultaneously and generate a single optimal design due to the trade-offs found in most practical problems (i.e., optimizing one response often leads to the degradation of another). Instead, MOP generates a set of "undominated" solutions from the multitude of feasible designs within the variable search space. This set is referred to as the Pareto front and depicted graphically for a two-objective problem in Figure 6. Mathematically, the Pareto front captures designs which cannot improve one objective function without degrading another and are therefore termed undominated solutions. It is the design engineer's role to then select one Pareto design which best suits their overall requirements. In MOWS, multiple objectives (n) are collapsed into a single function by assigning a weight (W_i) to each response:

$$f = \sum_i^n W_i \left(\frac{R_i - R_{i,target}}{R_{i,norm}} \right)^2 \qquad \text{Eq. (2)}$$

A normalization term ($R_{i,norm}$) is needed to account for responses with different orders of magnitude compared to others. The advantage of MOWS is that a single optimal design is generated. However, the solution is sensitive to weighing factors and care must be taken in ranking the importance of each response. The use of multiple objectives can be further generalized to targeting a time-dependent or transient response with TT. In this case, a single objective function is constructed using the root mean square error (RMSE) between

FIGURE 6 Basic optimization process and GA flowcharts.

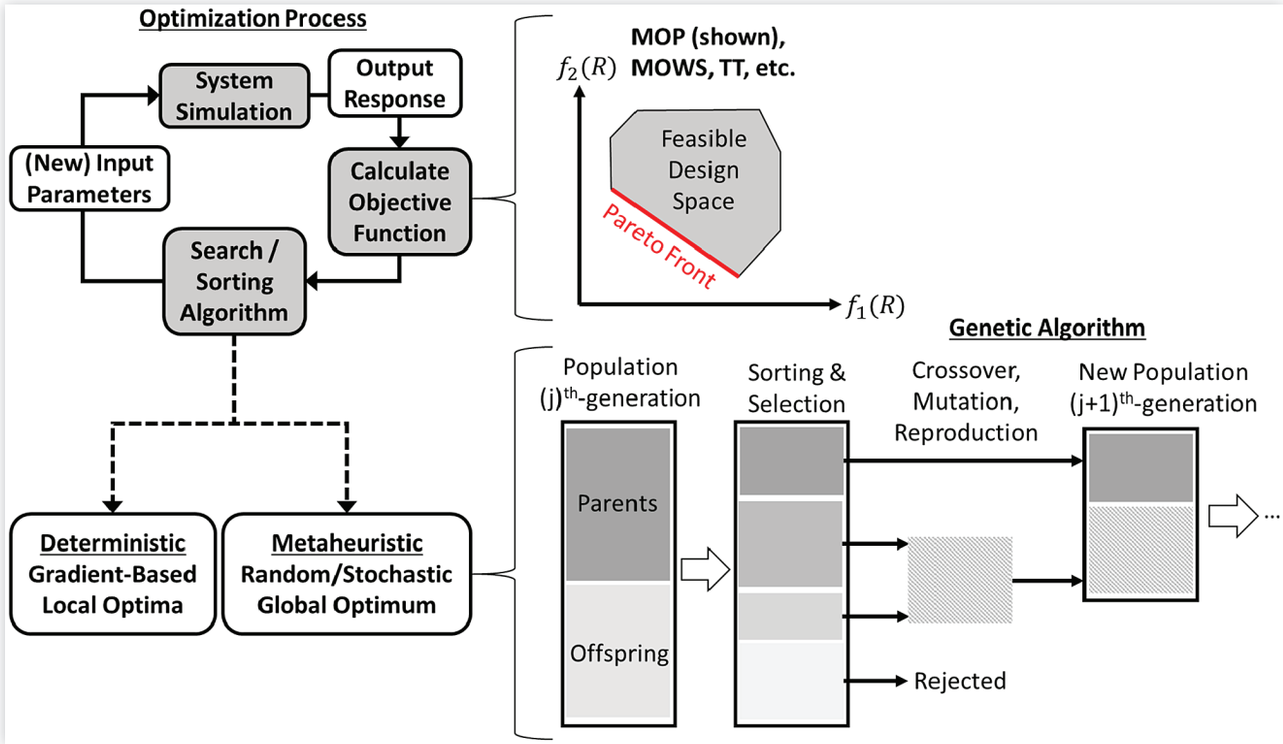

a transient response curve ($R(t)$) and a desired target profile ($R(t)_{target}$):

$$f = \sqrt{\frac{\int_{t_{inial}}^{t_{final}} \left(R(t) - R(t)_{target}\right)^2 dt}{\left(t_{final} - t_{initial}\right)}} \qquad \text{Eq. (3)}$$

Compared to MOP and MOWS, TT offers a convenient means of matching a desired injector ROI profile without having to specify individual responses that depend on the rate shape such as hydraulic duration, peak flow, and total injected quantity. Therefore, TT is ideally suited for determining the injector parameters needed to generate a desired rate shape.

Figure 6 shows that the design optimization process is iterative in nature. Minimizing the objective function(s) requires new combinations of input variables to be continually generated until the best possible design (i.e., global minimum) is identified. Genetic Algorithms (GAs) employ the principles of natural selection and evolution to achieve this task. At the most basic level, they work by selecting individual designs for subsequent crossover, mutation, and reproduction in the next generation based on some criteria for fitness [88, 89]. Deterministic search algorithms rely on calculus or gradient-based methods and tend towards local objective function optima, which may not represent the best possible design. However, GAs are metaheuristic search algorithms that are random or stochastic in nature and much more effective at capturing the true global optimum. These features have made GAs very useful for solving complex, multi-objective problems, including the design of gas turbines and GCI combustion systems [90, 91]. The Integrated Design Optimizer in GT-SUITE currently offers the Non-dominated Sorting Genetic Algorithm (NSGA-III) as a search algorithm [92]. This built-in tool was used along with MOP, MOWS, and TT objective function definitions to perform 1-D hydraulic model calibration and rate shape design.

3. Results and Discussion

3.1. Validation of Liquid Fuel Property Calculations

Figure 7 shows the discrepancy between the simulated versus measured liquid fuel properties for RON60 gasoline. Calculated values were determined using the methodology outlined in Section 2.6 and Aspen HYSYS as the chemical process software/property correlation database [74]. Each surface represents modeling error defined by the following percent difference formula (negative values correspond to an underprediction of measured data):

$$\text{Model error}\left(\%\ \text{difference}\right) = \frac{X_{Simulated} - X_{Measured}}{\text{Average}\left(X_{Simulated}, X_{Measured}\right)} \times 100\% \qquad \text{Eq. (4)}$$

FIGURE 7 Model error for RON60 liquid properties based on percent difference with measured data.

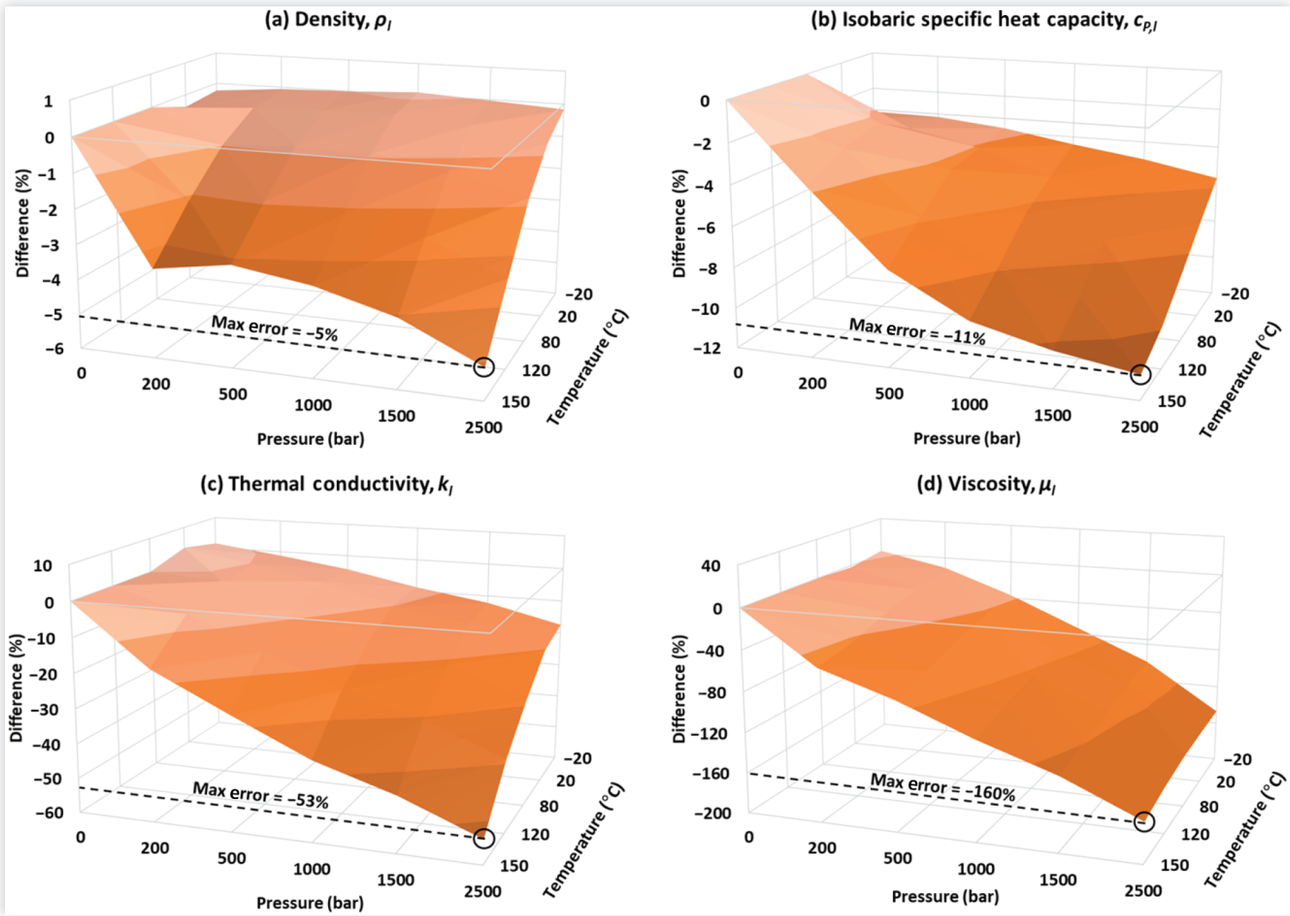

In general, Figure 7 indicates that the largest deviations occur at the highest temperature and pressure condition (i.e., 150°C and 2500 bar). Furthermore, the calculated values almost always underpredict the measured data, except for a few points of thermal conductivity at a pressure of 0 bar (gauge). Liquid density is extremely well reproduced by the RON60 gasoline model with less than −5% difference over the entire range. Isobaric specific heat capacity is also well captured with an error less than −11%. The agreement with measured data breaks down for thermal conductivity and viscosity, which show maximum errors of −53% and −160%, respectively. This is due to the lack of inherent μ_l and k_l versus pressure relationships within Aspen HYSYS (i.e., these properties are only treated as functions of temperature). All the measured versus modeled data for RON60 gasoline is tabulated in Appendix A.

Figure 8 shows that replacing the modeled viscosity and thermal conductivity values with measured data results in a difference of less than 0.3% for simulated injected quantity. This indicates that μ_l and k_l play a secondary role in the hydraulic model calculations. These findings are further substantiated in Figure 9 by the nearly identical ROI profile overlays generated using the measured versus modeled fuel data. The low sensitivity of hydraulic predictions to changes in liquid fuel viscosity and thermal conductivity could be explained by the lack of sub-models that rely explicitly on these properties. One example of such a model for μ_l would be estimating the viscous drag force on the main needle. Instead, the current 1-D injector model relies on implicit viscosity-flow relationships which are inherently less sensitive, such as the dependence of discharge coefficients or friction factors on Reynolds number.

As an alternative, empirical correlations from the literature could also be used to estimate the viscosity-pressure relationship of liquid hydrocarbons and improve fuel property model calculations. One relatively simple relationship relies on a reference viscosity at saturated conditions ($\mu_{l\,@\,Psat}$) and has shown very good agreement with experimental data for single compounds and mixtures [93]:

$$\left(\frac{\mu_l}{\mu_{l@P_{sat}}}\right) = \exp\left(m \times P\right), \quad m = 0.98 \times 10^{-5}\left(\text{kPa}\right)^{-1} \qquad \text{Eq. (5)}$$

FIGURE 8 Simulated total injected fuel quantities for the modeled versus measured RON60 liquid properties.

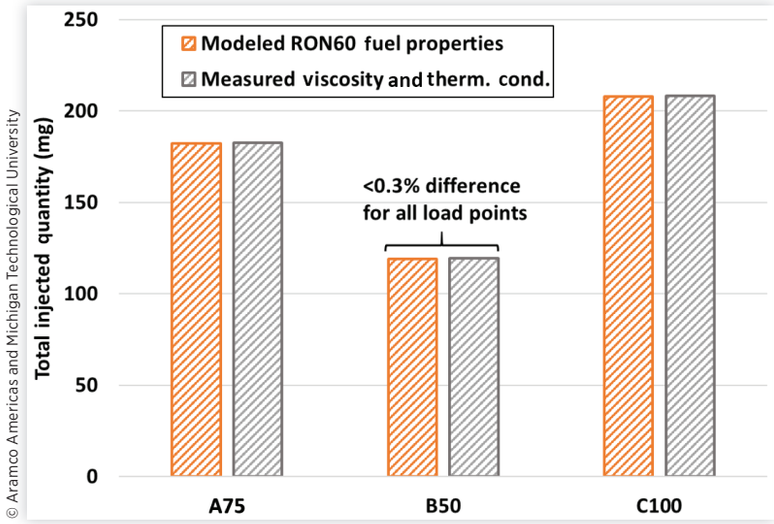

Figure 10 shows that the absolute maximum error in RON60 viscosity is reduced from 160% to 47% when employing Equation 5 to model pressure effects. Simple correlations such as these can be incorporated into Aspen HYSYS through a user-defined function to substantially improve fuel property model accuracy. Furthermore, the liquid viscosity of RON60 along its saturation pressure curve is a direct output from the HYSYS software, so no additional empirical data is needed to use this correlation. The updated viscosity values for RON60 based on Equation 5 are tabulated in Appendix A. Since the sensitivity of hydraulic model predictions to changes in μ_l and k_l was found to be extremely low (see Figures 8 and 9), all subsequent simulation results are reported for the original modeled fuel properties.

3.2. 1-D Hydraulic Injector Model Calibration for Gasoline

3.2.1. Initial Model Performance Figure 11 compares the simulated versus measured injected quantities for diesel and RON60 gasoline across all three load points. Error bars in the experimental data represent one standard deviation across three fresh injectors. Although an ISO 4113 fluid was used as a surrogate for diesel in the 1-D model, the total injected quantity is reproduced to within 3%. On the other hand, using a highly detailed surrogate to represent the physical properties of RON60 underpredicts fueling by

FIGURE 9 Simulated injector ROI profiles for the modeled versus measured RON60 liquid properties.

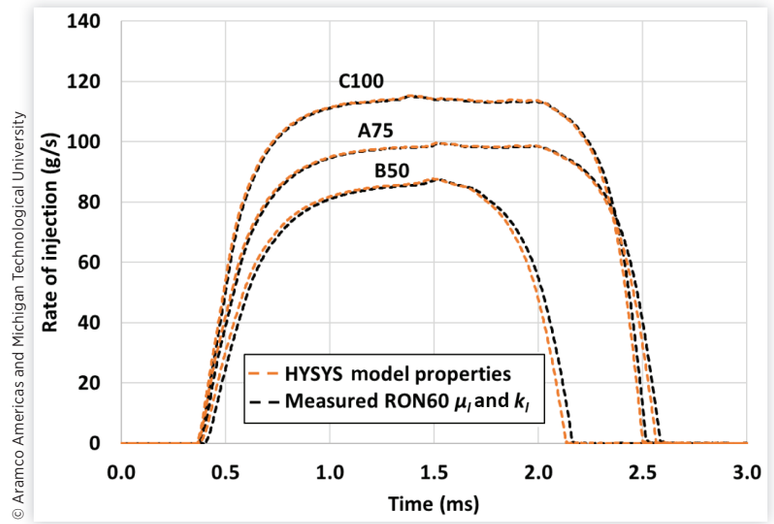

FIGURE 10 Model error for RON60 viscosity after using an empirical pressure correlation (Equation 5 [93]).

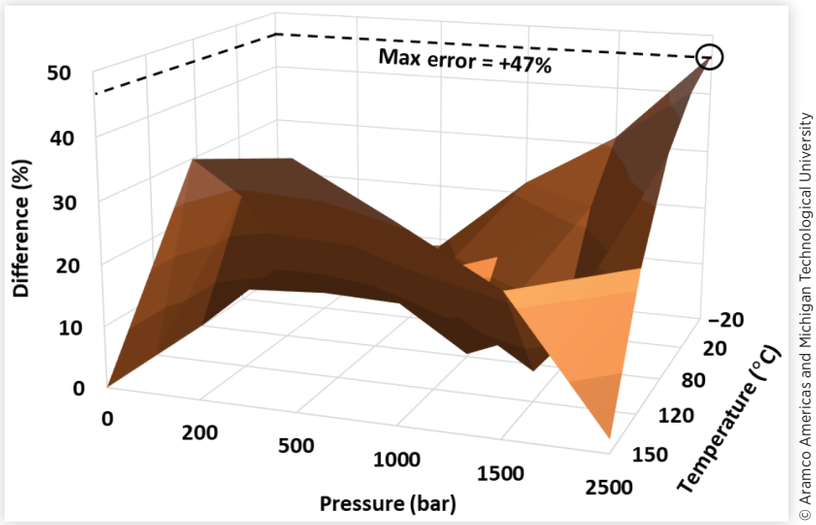

6-8%. Previous work has shown that this discrepancy is most likely due to retaining nondimensional flow coefficients from the original 1-D diesel model calibration [59]. Experimental and computational evidence was provided suggesting that discharge coefficients could increase for gasoline-like fuels because they operate at higher Reynolds number regimes compared to diesel in non-cavitating nozzle designs. Inaccurate fuel properties were also discussed as a possible contributor to the observed discrepancies, but was deemed as a minor factor given the good agreement between the measured and calculated physical properties [59]. The low error reported for the calculated ρ_l and $c_{P,l}$ at more representative thermodynamic conditions further substantiates this claim (see Section 3.1). Other properties that were not initially well captured by the RON60 gasoline fuel model, like μ_l and k_l, do not significantly impact the hydraulic model predictions.

Figures 12 and 13 compare the simulated versus measured ROI profiles for both fuels. Unlike the diesel data, RON60 predictions fall outside the experimental injector variation. As an example, the simulated peak flow at B50 is 3.9% lower than expected. This discrepancy cannot be fully explained even when the difference between the modeled versus actual RON60 density at injection conditions is considered. Equation 6 indicates that the deviation due to fuel density alone can only be as high as 2%:

$$\dot{m}_P = C_d A_o \sqrt{2\rho_f \Delta P} \rightarrow \frac{\dot{m}_{P,2}}{\dot{m}_{P,1}} = \sqrt{\frac{\rho_{f,meas}}{\rho_{f,sim}}} = \sqrt{\frac{760.7}{730.5}} = 1.02 \rightarrow 2\% \quad \text{Eq. (6)}$$

FIGURE 11 Simulated versus measured total injected fuel quantities across all load points.

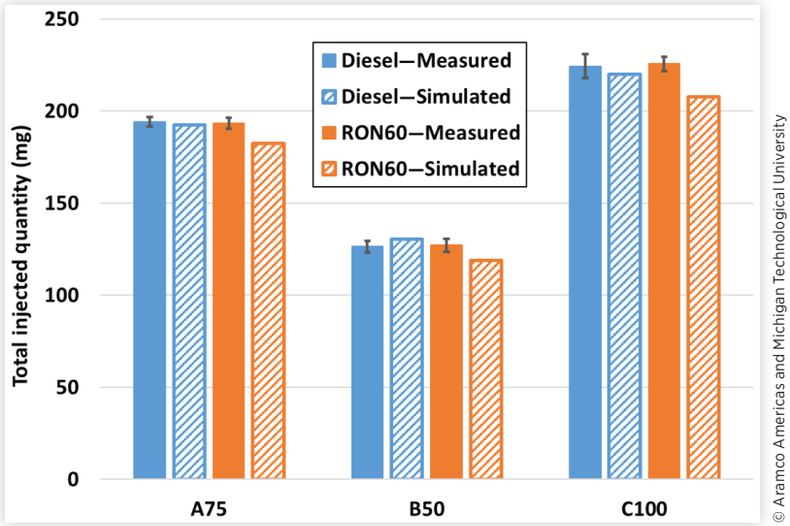

FIGURE 12 Simulated versus measured diesel ROI profiles.

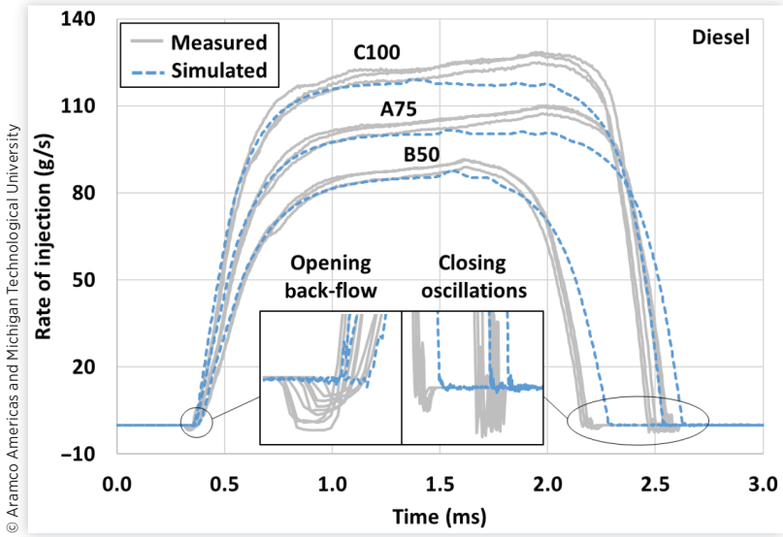

Therefore, the consistently underpredicted peak fueling rates suggest that 1-D model discharge coefficients should be increased to properly capture the performance of the RON60 gasoline. One major discrepancy between the simulated versus experimental ROI profiles shared by both fuels is the flat versus continuously rising steady flow pattern, especially at A75 and C100. However, previous work has demonstrated that this is most likely an artifact of using a simplified system-level model (i.e., a very simplified component layout upstream of the injector compared to the actual fuel system configuration shown in Figure 4) [59]. The slightly longer hydraulic durations predicted for diesel could also be attributed to this issue. Finally, neither fuel model could capture the reverse and oscillating flows observed at the start and end of injection, respectively. The current 1-D model does not account for the relaxation of the elastically deformed material, which is the most likely cause of these phenomena [94].

3.2.2. Calibration Parameters The only adjustable flow constants in the 1-D model are (i) maximum discharge coefficient of the ball-in-cone pilot valve ($C_{d,\ \max\ (BV)}$), (ii) maximum discharge coefficient of the main needle tip ($C_{d,\ \max\ (NT)}$), and (iii) contraction coefficient of the nozzle spray holes ($C_{c(NH)}$). These constants are part of specific component sub-models in GT-SUITE and used along with the instantaneous flow or geometric data to calculate the overall discharge coefficients (i.e., final C_d of the valves or nozzle holes at each time step). Table 4 summarizes the nominal discharge coefficient values used for diesel and the ranges considered in gasoline recalibration. Only values greater

FIGURE 13 Simulated versus measured RON60 gasoline ROI profiles.

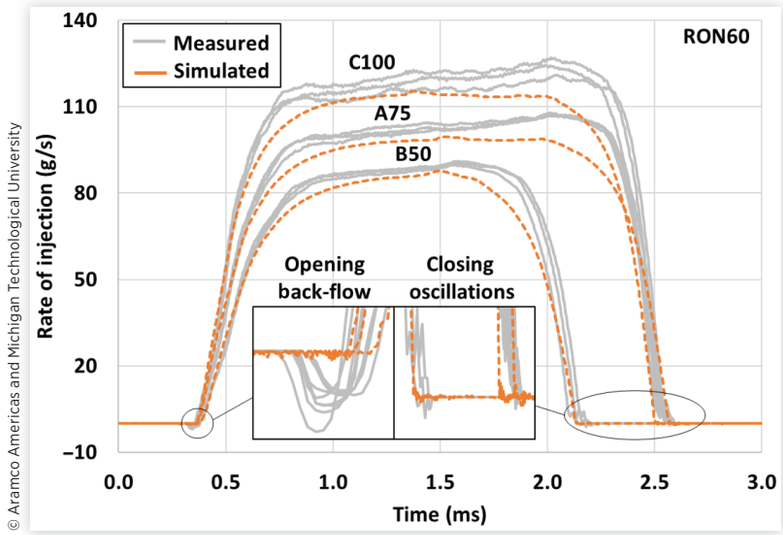

TABLE 4 Nondimensional flow coefficients adjusted during hydraulic model calibration.

Model coefficient	Nominal value (diesel)	Calibration range (RON60)
$C_{d,\,\max\,(BV)}$	0.85	0.85-0.99
$C_{d,\,\max\,(NT)}$	0.80	0.80-0.99
$C_{c(NH)}$	0.91	0.91-0.93

than the diesel baseline were investigated because RON60 required an increase in fueling rate to match the experimental data. The range of $C_{c(NH)}$ was capped at 0.93 because of a saturation effect observed in its ability to change the ROI profile. Parametric sweeps of the other coefficients showed that they remained effective at changing the ROI up to their theoretical limit (i.e., 0.99) [59].

3.2.3. Calibration Targets In the preceding study, a type of manual calibration was employed to determine the set of model discharge coefficients that best represented the measured RON60 performance [59]. However, this may not be feasible for complex models with more than three parameters. The current work, therefore, generalizes this process by using multi-objective optimization. Input parameters consisted of the three discharge coefficients in Table 4. Figure 14 shows that for MOP and MOWS, only three specific responses were chosen among the variety describing ROI: (i) total injected quantity, (ii) hydraulic duration, and (iii) maximum needle velocity. The total injected quantity and hydraulic duration combine to constrain the rate shape without the need to target the opening or closing ramp. Parametric sweeps of the discharge coefficients revealed that they have a negligible impact on hydraulic opening delay and timing of the pilot valve bounce feature, so these responses were ignored. However, the timing of the maximum needle lift feature can change significantly when $C_{d,\,\max\,(BV)}$ is adjusted. This feature is related to main needle dynamics and should be accurately reproduced by the 1-D model. Although not available as an explicit response to target within GT-SUITE, the timing of this event can be implicitly correlated to the maximum needle opening velocity.

Figure 15 shows the simulated max needle opening velocity versus timing of the maximum needle opening feature for RON60 gasoline. These plots were generated from parametric sweeps of $C_{d,\,\max\,(BV)}$ between 0.7 and 0.99 while keeping all other discharge coefficients at their nominal value (see Table 4). Increasing $C_{d,\,\max\,(BV)}$ leads to higher flow through the pilot valve during opening, more rapid development of the force imbalance driving needle lift, and faster needle opening velocity. Corresponding calibration targets were determined by relating the experimentally observed onset of the maximum needle lift to the simulated maximum opening velocity (dashed black lines). Alternatively, the desired maximum velocity targets could have been extracted from the measured needle lift profiles of RON60 [95, 96]. However, the existing data set does not cover all the injection conditions used in this study.

For MOP and MOWS, all response targets were specified using a single average value extracted from the three injector measurements. Each load point was considered equally important and given an equal case weight to cover the injector operating range fairly. Additionally, the weight factors for MOWS were evenly distributed among each response. The definition of targets for TT was comparatively simple and only required importing the experimental RON60 ROI profiles from each measured injector into GT-SUITE. Analogous to setting even MOP and MOWS case weights, all three SET points were considered simultaneously during TT optimization to

FIGURE 14 ROI response features used during MOP and MOWS parameter calibration.

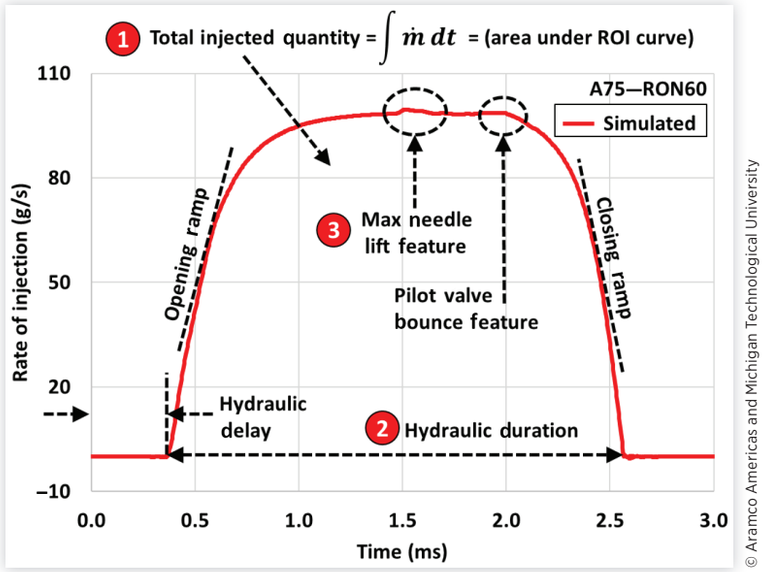

FIGURE 15 Simulated maximum needle lift velocity versus experimental onset of the maximum needle lift feature.

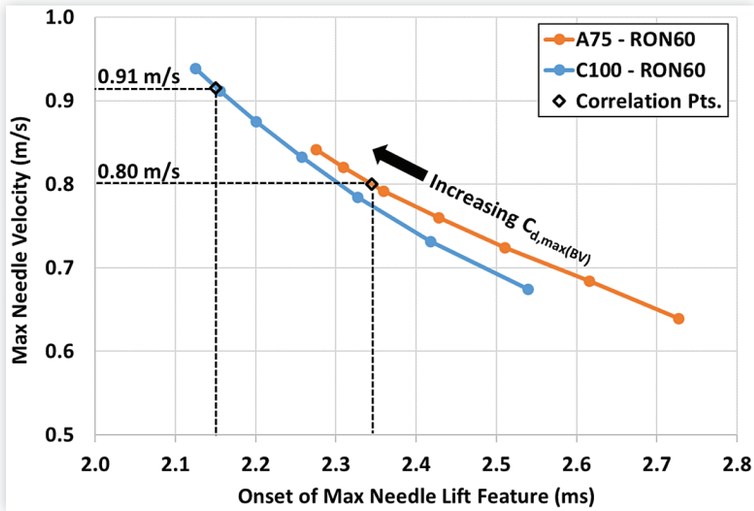

determine one set of discharge coefficients that would capture gasoline performance over the entire operating range. Finally, the default GA settings were selected in GT-SUITE (i.e., a calculated population size of 16 based on the number of calibration parameters, cases, etc., and a fixed setting of 15 generations). Table 5 summarizes all the target and optimization settings used to calibrate the discharge coefficients.

3.2.4. Calibrated Model Performance

Table 6 compares the simulated injected quantities for each calibration method to the experimental RON60 data. The RSME across all SET points clearly demonstrates an improved model closure for the optimization-based techniques. All three methods resulted in similar predictions and indicate that any of them could be used for calibration. MOP had the lowest RMSE and is thus considered the "best" calibration. The slightly better closure of MOP compared to TT may be due to the GA being optimized for Pareto sorting and ranking [88, 90]. MOWS performance could potentially be improved by considering different weight factors. Figure 16 summarizes the progression of model closure with experimental injected quantity data starting from the nominal, uncalibrated model using detailed RON60 properties (RON60—No Calibration) to the manual calibration technique employed in prior work (Original Calibration) [59], and, finally, the best calibration result obtained with MOP optimization. With this last approach, the RON60 injector model was able to achieve less than 3% difference across all three load points, making its performance equivalent to the original diesel model.

Figure 17 shows that the MOP calibration can accurately reproduce individual ROI profiles as well. Compared to the uncalibrated model with nominal (i.e., diesel) discharge coefficients, the MOP optimization demonstrates improved closure on both hydraulic duration and peak flow for RON60 gasoline. Other specific hydraulic features, such as the timing of the maximum needle lift and pilot valve closing bounce, are also well preserved in the MOP simulations, indicating that the correct response targets were chosen. As previously mentioned, the discrepancy between relatively flat (predicted) versus slightly rising (experimental) ROI profiles near the end of injection is not a result of poor simulation fidelity but an artifact of using a simplified system-level model upstream of the injector.

Figure 18 indicates that the MOP calibration captures RON60 gain curves more accurately than the uncalibrated model above 1500 bar. Agreement tends to break down below this point likely because of the restricted calibration range defined by A75, B50, and C100, all of which have injection pressures at or above 1500 bar (see Table 2). Additional high-fidelity ROI profiles down to idling fuel pressure (400 bar) would be needed to support a more comprehensive calibration covering the entire engine operating range.

Experimental needle lift profiles are shown in Figure 19. Measurements were conducted using high-resolution X-ray computed tomography scans (±2 μm) at the Advanced Photon Source (APS), Argonne National Laboratory, and have been described elsewhere [66, 95, 96]. Results indicate that RON60 gasoline has faster injector needle opening and closing rates compared to diesel. Corresponding simulations using both the uncalibrated and MOP calibrated RON60 models are shown in Figure 20. Although the relative fuel effect on the closing rate is well predicted, the faster RON60 opening rate

TABLE 5 Summary of MOP and MOWS response targets used for RON60 gasoline model calibration.

Case	Injected quantity (mg)	Hydraulic duration (ms)	Maximum needle lift velocity (m/s)	MOP & MOWS case weights
A75	193	2.15	0.80	1.0
B50	127	1.75	0.63	1.0
C100	226	2.16	0.91	1.0
MOWS W_i	1.0	1.0	1.0	—

TABLE 6 Total simulated injected quantities for each calibration method versus experimental data.

Case	Experiment (mg)	RON60 no calibration	Original calibration	MOP	MOWS	TT
A75	193.3	182.4	189.2	193.3	193.8	193.2
B50	127.1	118.9	126.1	128.7	130.6	128.1
C100	225.6	207.8	215.8	220.2	220.8	220.0
RMSE	—	12.96	6.16	3.20	3.45	3.24

is not as prominent as the experimental data indicates. Furthermore, the measured trends of the increasing opening rate difference between fuels and the degree to which the peak needle lift changes as a function of injection pressure are not reproduced in simulation.

The measured needle lift profiles were not directly used to help calibrate the 1-D gasoline model due to a limited understanding of these differences. For example, peak lift was set as a constant value of 610 µm in the model and based on standard X-ray computed tomography scans made at a resolution of 10-15 µm. This level of measurement uncertainty does not account for the much lower travel distances of 450-500 µm observed in the experiments. One possible explanation could be the lack of an appropriate friction or viscous drag sub-model for the main needle. Viscosity impacts the flow dynamics, discharge coefficients, and the transient development of pressure gradients that drive needle motion. However, it also contributes to the friction and drag experienced by the needle as it moves through fluid. This aspect of needle physics was not necessary for good performance of the nominal diesel injector model, but could be critical for capturing the nuanced fuel effects exhibited by gasoline.

Figure 21 shows the hydraulic opening and closing delays for RON60 gasoline. Opening delay is defined as the time between electronic driving signal initiation and when fuel begins to emerge from the injector. Closing delay is defined as the time between electronic signal shut-off and when fuel flow ceases. The MOP calibration results agree very well with experimental data, except for C100 where the difference is 140 µs and relatively large. One possible explanation for this discrepancy is the unrepresentative cavitation modeling of the control chamber inlet orifice. Under heavily cavitating conditions, liquid flow through the orifice would decrease, thereby lengthening the needle closing delay (refer to Figure 3 for the relationship between the orifice flow and v_{close}). This phenomenon would be most prominent for volatile fuels operating at high injection pressures (i.e., RON60 at the C100 condition). Although both control chamber orifices were specified as "cavitating" in GT-SUITE, the sub-model may not have fully captured the extent of cavitation and its impact on needle closing velocity at this extreme condition.

The nondimensional flow coefficients determined using different calibration methods are compared to nominal diesel values in Table 7. Results from the optimization-based techniques are consistent with the original manual calibration performed in prior work and align with previous experimental data, suggesting that C_d can rise when using gasoline-like fuels with these types of nozzle orifices [59]. One notable trend in Table 7 is the convergence of $C_{C(NH)}$ to a value of 0.93. The impact of this coefficient on the ROI was found to saturate at this value, providing a clear upper limit during calibration. $C_{d,\,\max\,(NT)}$ is also considerably higher for the MOP, MOWS,

FIGURE 16 Progression of the simulated injected quantity closure with experimental data for different calibration approaches.

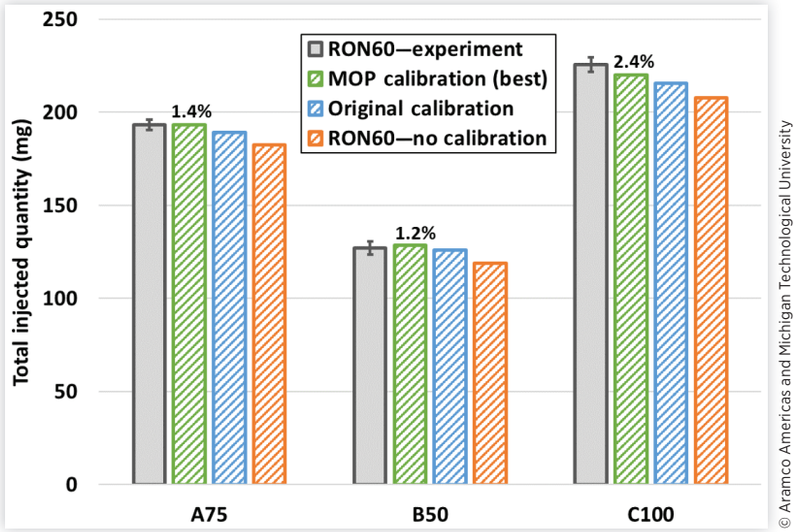

FIGURE 17 Simulated RON60 gasoline ROI curves versus experimental data for different calibration approaches.

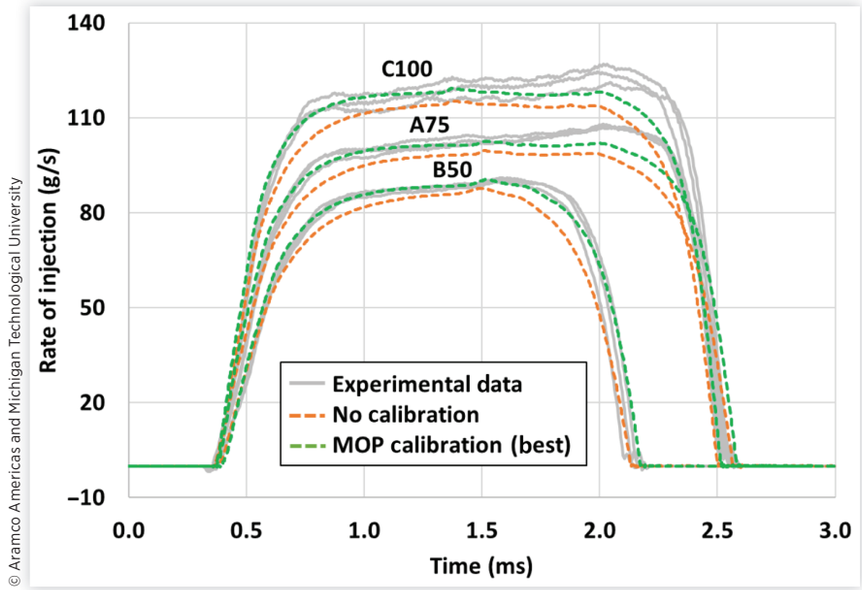

FIGURE 18 Simulated RON60 gasoline gain curves versus experimental data for different calibration approaches.

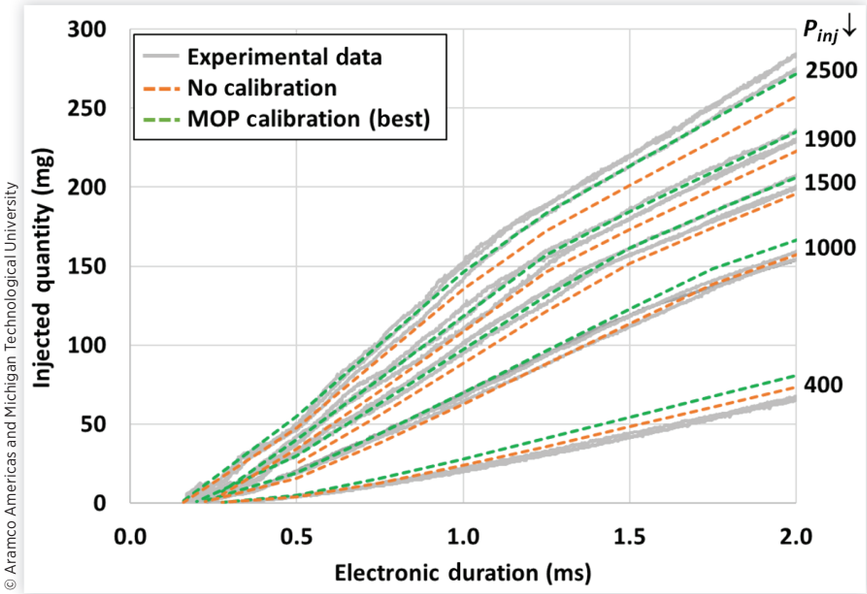

FIGURE 19 Experimental diesel and RON60 gasoline needle lift profiles.

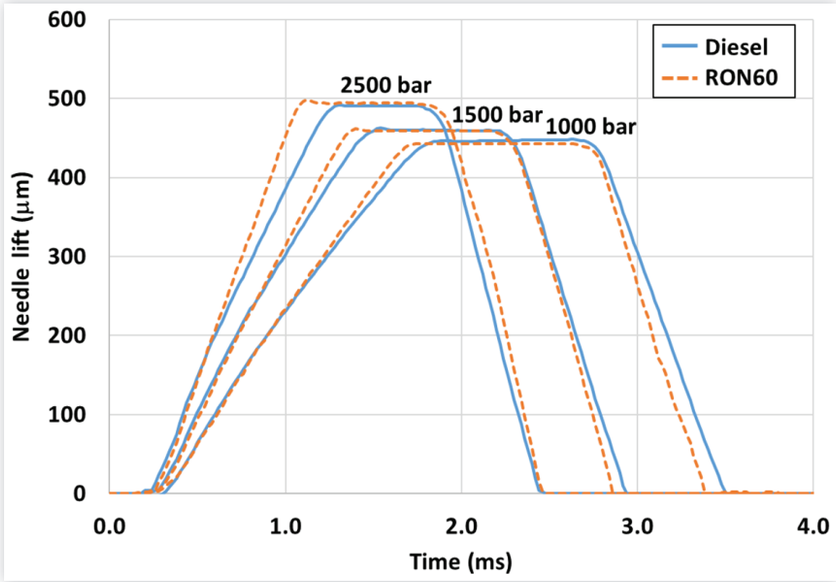

FIGURE 20 Simulated diesel and RON60 gasoline needle lift profiles for different calibration approaches.

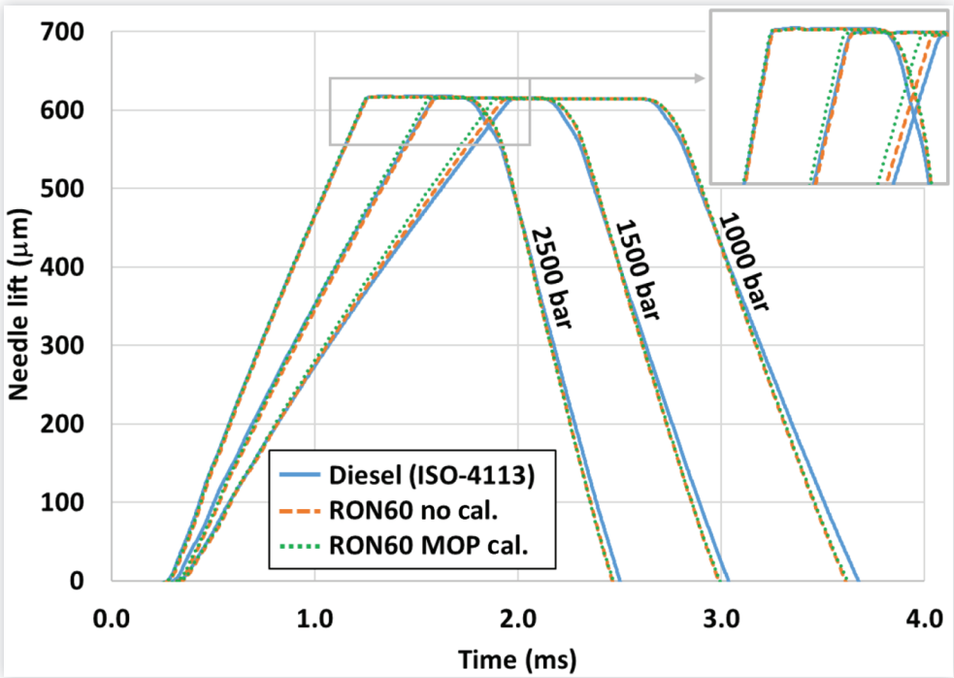

FIGURE 21 Simulated versus experimental hydraulic opening and closing delays for RON60 gasoline.

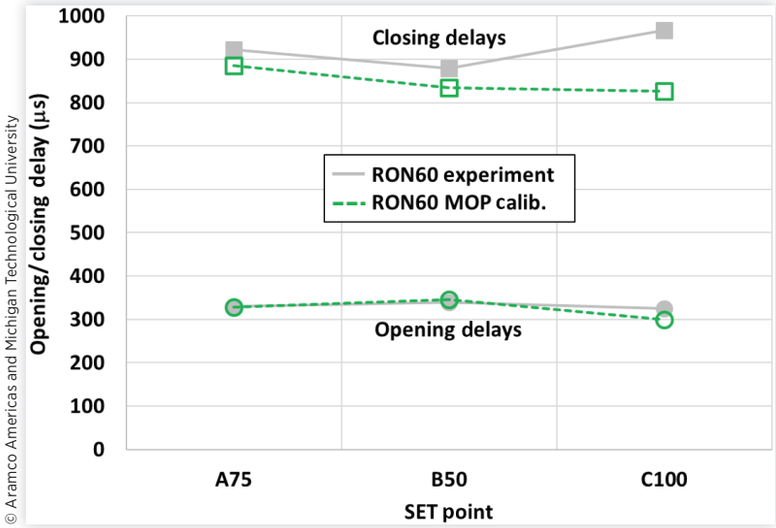

and TT calibrations compared to the original calibration. This is most likely due to setting an overall tolerance of only 5% for the agreement between the measured and simulated results in the original calibration versus the current objective function minimization.

3.3. Rate Shape Design Using Calibrated 1-D Hydraulic Gasoline Injector Model

3.3.1. Rate Shape Target Since the detailed injector simulation was not coupled to a predictive combustion model, it could not be used to design rate shapes based on engine performance and emissions targets like brake thermal efficiency or engine-out NOx. Instead, the focus of this study was to understand what standard injector parameters contribute to changing the rate shape and how a desired ROI profile might be achieved using the optimization approaches available in GT-SUITE.

To help reduce the optimization problem complexity (i.e., input parameter search space) and shorten the computational runtime, only single continuous injection events were considered. This situation is far simpler than a digital rate shaping approach, which would require additional parameters such as the number of injections, dwell time between injections, and injection quantity splits to be included. Since it is also not possible to determine the potential negative impact on burn duration caused by multiple fuel pulses or extended durations without a coupled combustion model, the hydraulic duration was simply constrained to the same value observed during stock injector operation.

Figure 22 shows an idealized ROI target for the B50 operating point. A triangular or "ramped" rate shape was chosen to demonstrate a potential pathway for lowering NOx emissions. The kinetics of NOx formation are extremely sensitive to temperature and depend on the amount of heat released early in the combustion process. Therefore, any method that reduces initial heat release rates, such as slowing down the rate of fuel injection, also reduces peak charge temperatures and NOx emissions. The practical use of slow injection opening ramps to reduce NOx has been previously documented and discussed [30, 33, 36, 53, 54]. This technique could work synergistically with a standard lean aftertreatment system and the improved soot-NOx trade-off of GCI versus diesel to help meet future ultralow-NOx emissions regulations. First, the simulated ROI profile was used to extract a hydraulic duration (Δt = 1.78 ms) and determine the total injected fuel quantity (m_T = 128.7 mg). Next, an idealized triangular shape was constructed by requiring that it achieve the same fuel quantity (area under ROI curve) over the same duration as the original profile. This essentially translates into calculating a new peak fueling rate for the desired shape based

TABLE 7 Nondimensional injector model flow coefficients determined using different calibration methods.

Model coefficient	Nominal values (diesel)	Original calibration	MOP	MOWS	TT
$C_{d,\,\max\,(BV)}$	0.85	0.90	0.898	0.923	0.891
$C_{d,\,\max\,(NT)}$	0.80	0.88	0.984	0.970	0.986
$C_{c(NH)}$	0.91	0.93	0.928	0.929	0.929

FIGURE 22 Determination of idealized triangular or "ramped" rate shape profile for RON60 gasoline at B50.

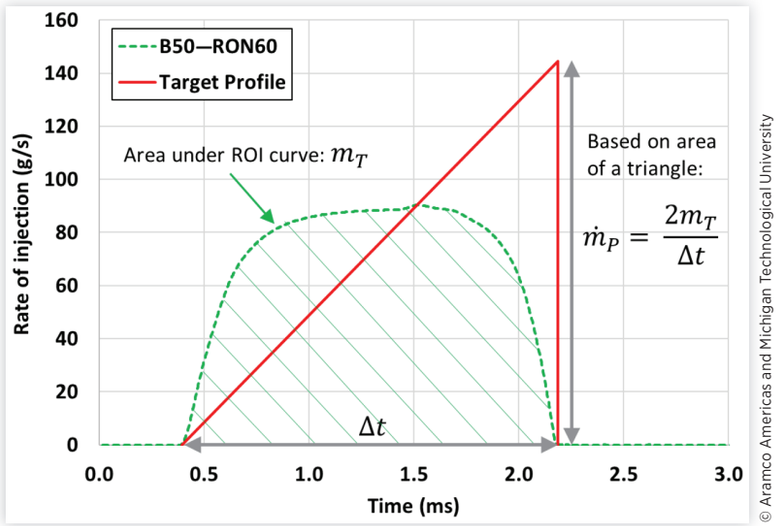

on the area of a triangle ($\dot{m}_p$ = 144.6 g/s). A very sharp closing ramp was also kept in the target since it can help produce a strong post-injection entrainment wave and potentially mitigate soot [48].

3.3.2. Hydraulic Parameter Sweeps Figure 3 highlights the various parameters that impact the rate shape for a standard common rail injector. This section will examine how each of these can be modified using a calibrated 1-D gasoline model to achieve the target ROI profile in Figure 22. Realistic search spaces will also be specified for each variable to adequately constrain the objective function minimization problem. Electronic injector driving parameters such as hold current and boost voltage were excluded because they have a relatively minor impact on the ROI compared to hydraulic design features for this type of hardware [40]. Parameters including nozzle K-factor and inlet hole edge curvature cannot be directly studied using a 1-D model and are better suited for exploration with detailed three-dimensional (3-D) computational fluid dynamics (CFD) models focused on in-nozzle flow behavior [97, 98]. Therefore, these were excluded from the current investigation.

3.3.2.1. Control Chamber Inlet Orifice Diameter (D_{in}). The main needle opening and closing velocities are both influenced by the inlet orifice (see description of v_{open} and v_{close} in Figure 3) [40]. Figure 23 shows the ROI profiles corresponding to -40/+20% changes in diameter and highlights the strong sensitivity. An increase in D_{in} leads to a reduced control chamber draining rate when the pilot valve

FIGURE 23 RON60 gasoline rate shape versus control chamber inlet orifice diameter (D_{in}) at B50.

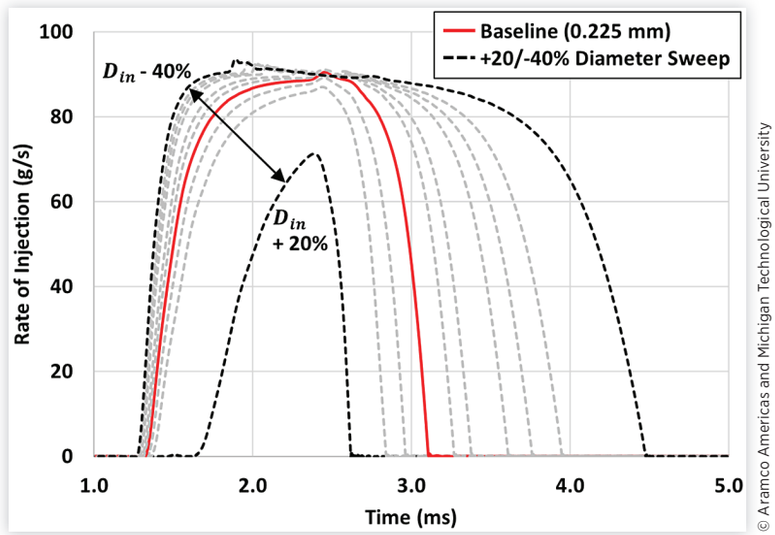

is open ($Q_{outlet} - Q_{inlet}$), slower needle lift velocity (v_{open}), and shallower initial ROI. This helps to create a somewhat triangular rate shape which aligns with the desired profile. Increasing the inlet orifice diameter beyond 20%results in no injection event because the reduced force imbalance generated is not enough to unseat the needle.

3.3.2.2. Control Chamber Outlet Orifice Diameter (D_{out}). Only the main needle opening velocity is significantly influenced by the outlet orifice [17, 40]. Figure 24 shows the ROI profiles corresponding to +40/−25% changes in diameter and indicates a similar level of sensitivity as the inlet orifice. Decreasing D_{out} leads to a reduced control chamber draining rate when the pilot valve is open ($Q_{outlet} - Q_{inlet}$), lower needle opening velocity (v_{open}), and shallower initial ROI, all of which align with the target profile. Since changes to the outlet orifice diameter suggest even slower initial ROIs compared to D_{in}, it should be possible to achieve the desired rate shape by changing only D_{out}. Decreasing the outlet diameter by more than 25% results in no injection event because the inlet versus outlet flows through the control chamber become balanced and do not result in a fluid volume change. Thus D_{out} was only considered between its baseline diameter −25%.

3.3.2.3. Total Nozzle Area (A_o). Although the changes to control chamber inlet/outlet orifices discussed above can produce triangular rate shapes, they do so at severely reduced peak flows. Since A_o is directly proportional to the steady mass flow rate, increasing the nozzle hole diameter (D_o) or total number of nozzle holes (N) should provide a means of increasing the peak fueling:

$$\dot{m}_p = C_d A_o \sqrt{2\rho_f \Delta P} \rightarrow A_o = N\frac{\pi D_o^2}{4} \qquad \text{Eq. (7)}$$

However, the results in Figure 25 indicate that a three times (3×) increase in A_o does not correspond to a 3× increase in peak mass flow rate compared to the baseline. This is due to rapid draining and depressurization of fuel within the nozzle sac volume (i.e., a counteracting decrease of ΔP in Equation 7). Figure 26 highlights the drastic reduction in nozzle sac pressure that accompanies an isolated increase in A_o. Therefore, total nozzle area must be increased in tandem with other internal hydraulic parameters to maintain ΔP [9]. Prior studies using the same injector demonstrated that a 3.2× increase in peak baseline flow could be achieved through a combination of nozzle hole diameter and internal hydraulic parameter modifications [99]. This provided a reasonable upper limit on changing A_o within the current investigation.

3.3.2.4. Rail Pressure. One possible way to increase the sac pressure is to increase the upstream rail pressure. As shown in Equation 7 and Figure 27, the increase in peak flow is proportional to $\sqrt{\Delta P}$ and not enough to achieve the target value even at the maximum available system pressure of 2500 bar. Furthermore, raising the rail pressure increases the initial ROI and could negatively impact the brake engine efficiency through larger parasitic losses. Since these are undesired effects, the rail pressure at a given operating point was maintained at its original value (see Table 2).

3.3.2.5. Nozzle Sac Diameter (D_{sac}). The filling and draining rates of fuel within the nozzle sac are influenced by its geometry and have an impact on injection ΔP across the spray holes. Increasing the nozzle sac diameter effectively makes the sac volume larger and should lead to prolonged filling times, slower pressure development, and reduced opening ROI. At the end of injection, it is expected to take longer for depressurization, leading to a slower closing ROI. However, Figure 28 shows the exact opposite behavior. This could be explained by the simultaneous counteracting effect

FIGURE 24 RON60 gasoline rate shape versus control chamber outlet orifice diameter (D_{out}) at B50.

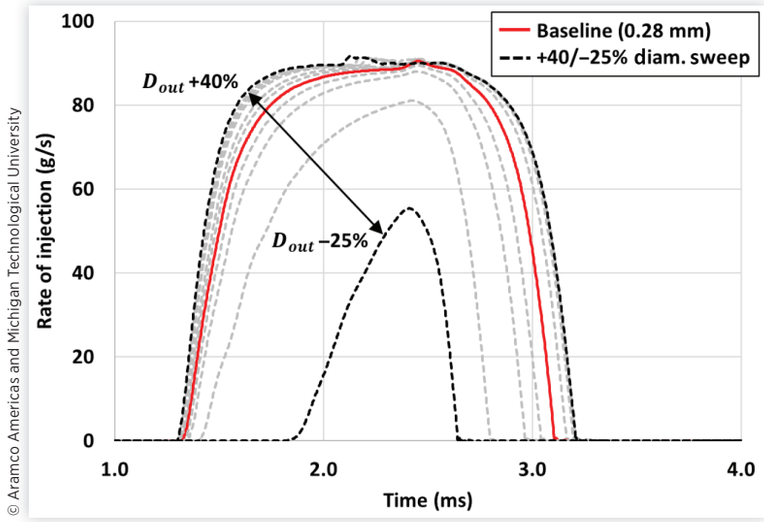

FIGURE 25 RON60 gasoline rate shape versus the total nozzle area (A_o) and corresponding nozzle exit hole diameter (D_o) at B50.

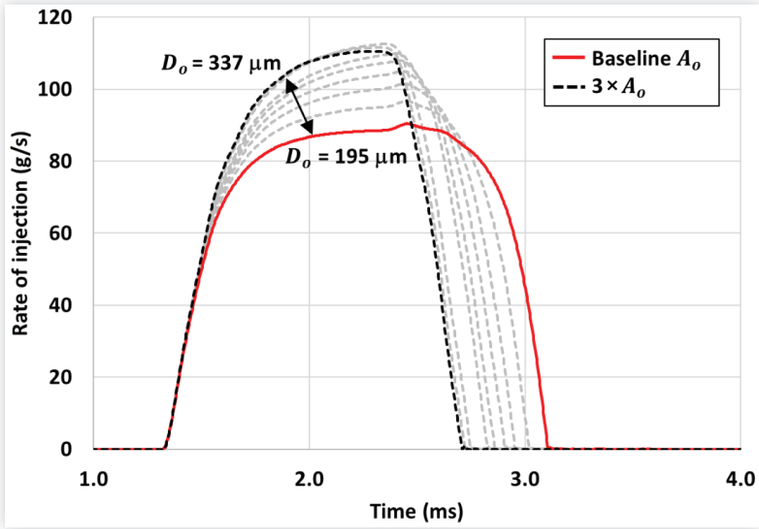

of decreased needle seat flow throttling. As D_{sac} increases, the length, throttling losses, and pressure drop across the needle seat are also reduced leading to a more rapid pressure buildup and release rates in the sac. The opposite effect is observed when the nozzle sac diameter is decreased because the seat length is increased. Since this parameter does not contribute to a triangular rate shape profile, it was excluded from consideration.

3.3.2.6. Needle Seat Half-Angle. Increasing the needle tip angle generates a higher effective seat flow area for a given amount of lift. Figure 29 shows that this leads to higher ROIs at the start of injection (SOI). Conversely, decreasing the half-angle reduces the effective flow area and creates slower opening ramps that are aligned with the target rate shape. However, the slower opening profiles are accompanied by undesirable slower closing rates. Modifying the needle shape or sac geometry can also change the in-nozzle flow dynamics and ultimately impact the discharge coefficient [29]. Since 3-D CFD models are better suited to understand these effects, both the needle half-angle and sac geometry were excluded from the optimization search space.

FIGURE 26 RON60 gasoline sac pressure versus the total nozzle area (A_o) and corresponding nozzle exit hole diameter (D_o) at B50.

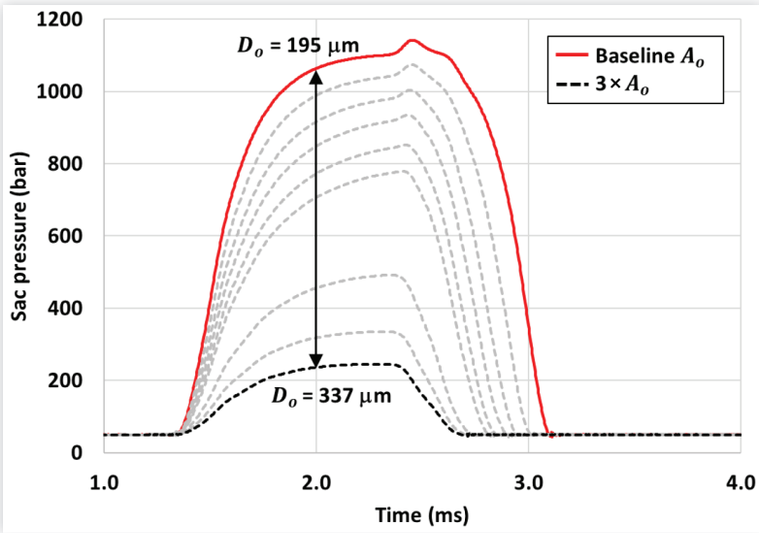

FIGURE 27 RON60 gasoline rate shape versus rail pressure at B50.

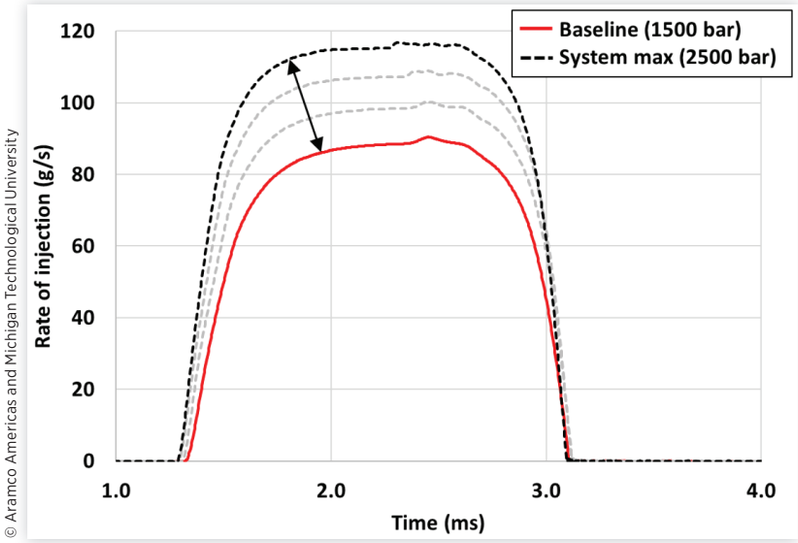

3.3.2.7. Needle Orifice Diameter (D_{NO}). Another way to maintain sac pressure during high flow injection events is to reduce fuel supply throttling. This essentially translates into increasing the needle orifice diameter. Figure 30 shows that a substantial amount of flow capacity can be recovered by increasing D_{NO} at 3× the baseline total nozzle area. The new peak flow saturates between diameters of 2.8-3.4 mm and becomes roughly 2.2× the baseline value, which is much closer to the theoretical expectation. To avoid ROI fluctuations generated near the peak flow limit, the upper bound of D_{NO} was constrained to a maximum of 2.4 mm.

Table 8 summarizes the final parameter search space used for the rate shape targeting exercise. In addition to the total nozzle area, the corresponding exit nozzle hole diameter range is also listed. The energizing time (ET) was varied across the durations observed over the entire B-speed load range (i.e., B25 to B100). The upper limit prevented excessively long durations which could contribute to degraded combustion efficiency in the real application. Figure 24 indicates that decreasing D_{out} to achieve a triangular rate shape significantly impacts the hydraulic opening delay. Since the SOI can easily be adjusted in the real engine application to compensate, this was not considered as a critical optimization or target parameter. Finally, although every hydraulic parameter discussed in this section could have been included in the objective function minimization search space, the number of variables

FIGURE 28 RON60 gasoline rate shape versus nozzle sac diameter (D_{sac}) at B50.

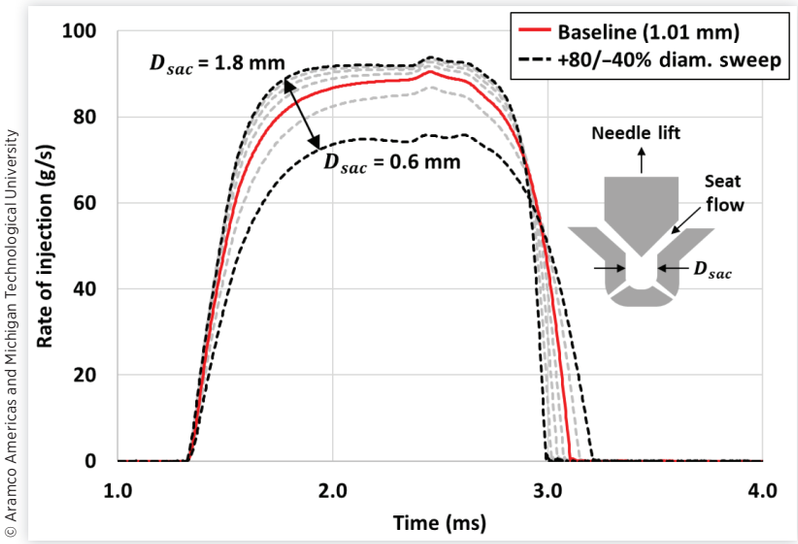

FIGURE 29 RON60 gasoline rate shape versus the main needle seat half-angle at B50.

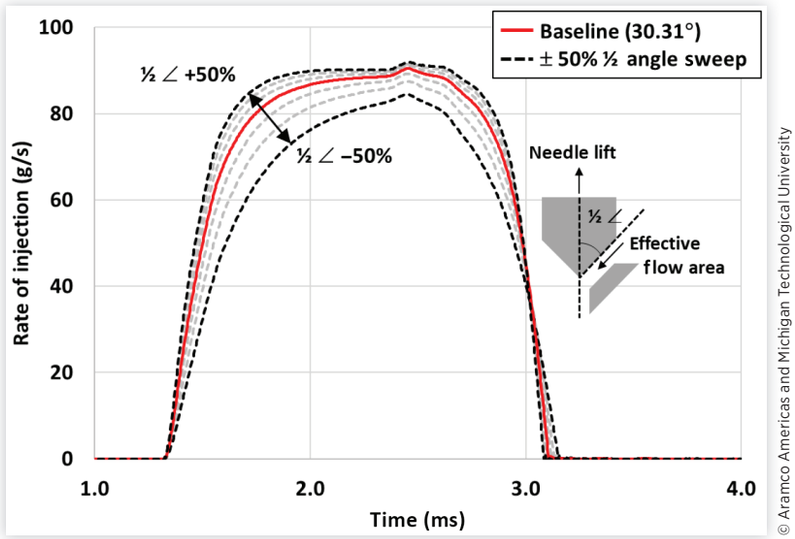

was systematically reduced and their ranges constrained based on fundamental injector behavior. This was done to help achieve reasonable computational runtimes.

3.3.3. Rate Shape Matching A TT objective function definition was used to determine the optimal set of parameters from Table 8. This option provided the most convenient rate shape target specification in GT-SUITE and was previously shown to be as effective as MOP or MOWS in matching ROI (see Table 6). To ensure that objective function minimization was reached, the number of generations in the GA was increased beyond its default. Table 9 indicates that increasing the generations above 15 does not produce any further reduction in objective function value and confirms the default setting was valid.

A full-factorial DoE was also carried out using the same design variables in Table 8 and served as a comparative benchmark. The optimal solution was determined by evaluating each DoE simulation with the following custom error function and choosing the result with the lowest RMSE:

$$RMSE_{DoE} = \sqrt{\frac{\left(\delta_{\text{Peak ROI}}\right)^2 + \left(\delta_{\text{Opening Ramp}}\right)^2}{2}},$$
$$\delta_i = \left|\frac{X_{\text{Simulated}} - X_{\text{Target}}}{X_{\text{Target}}}\right| \cdot 100\% \qquad \text{Eq. (8)}$$

FIGURE 30 RON60 gasoline rate shape versus needle orifice diameter (D_{NO}) for 3× A_o at B50.

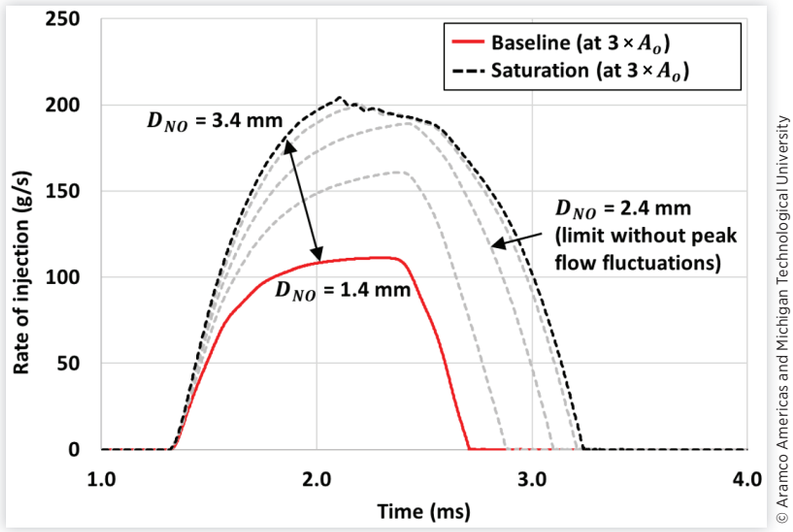

TABLE 8 Rate shape targeting optimization parameters and ranges.

Optimization parameter	Minimum value	Maximum value
D_{out} (mm)	0.21	0.28
A_o (X Baseline)	1.0	3.0
$D_o^{(1)}$ (μm)	195	338
D_{NO} (mm)	1.4	2.4
ET (ms)	1.23	1.79

Notes: (1) Nozzle exit hole diameter is not a separate variable but related to total nozzle area through Equation 4.

Equation 8 indicates that only peak injection rate (X_{Target} = 144.6 mg/ms) and initial ROI opening slope (X_{Target} = 82.6 mg/ms^2) were used to quantify target matching with the simulated results ($X_{\text{Simulated}}$). Other possible criteria, such as hydraulic delay or duration, were not considered because the SOI and ET can easily be adjusted to meet the desired combination of injection timing and fueling quantity.

Optimal TT and DoE solutions are compared against the target rate shape in Figure 31. The desired profile could not be exactly matched due to limitations in the rate shaping flexibility of standard DI injectors and the constrained variable search space considered in this preliminary study. Alternative hardware configurations, such as direct-acting piezo injectors, could be used to achieve the desired ROI profile more closely [30, 31]. Piezo injectors can control needle lift through an applied voltage signal and achieve highly variable rate shapes, although additional robustness and cost concerns would need to be addressed for practical implementation. Nonetheless, the TT method provided a roughly triangular rate shape with a slow opening and fast closing dynamics approaching the idealized ROI. The full-factorial DoE had 2160 simulations and yielded very similar results when using the average, fully developed ROI opening slope between 0 g/s and 30 g/s. The actual optimal case outputs from both TT and DoE methods had slightly lower total injected fuel quantities than the target profile. This was most likely due to the lack of a specific quantity target, as in the case of MOP or MOWS. The ET for each solution was thus slightly adjusted to provide the results reported in Figure 31.

As expected from the parametric sweeps, Table 10 indicates that a decrease in control chamber outlet orifice diameter accompanied by an increase in spray hole and needle orifice diameter was required to achieve a triangular rate shape. Furthermore, the TT objective function coupled to a genetic search algorithm showed a substantial computational runtime reduction compared to a full DoE.

Permanently shifting the ROI to achieve a potentially low-NOx result has repercussions on other aspects of combustion performance. For example, a triangular rate shape could prolong the burn duration and lead to a deterioration in engine thermal efficiency [36, 53, 54]. As shown in Figure 32, the spray momentum flux was also affected, which could lead to a reduced spray penetration, slower mixing rates, and suboptimal spray-wall interaction for a specific piston bowl geometry. Furthermore, an ROI profile that works well at medium to high loads like B50 may not be desirable at lower loads. The corresponding design changes listed in Table 10 could even inhibit a proper injector operation at such conditions (i.e., no injection event at idle). With these considerations in mind, it is important that a real rate shaping design exercise include predictive combustion modeling and the entire engine operating range so that all trade-offs can be accounted for during optimization.

4. Summary and Conclusions

A 1-D hydraulic model was developed in GT-SUITE for a production heavy-duty diesel injector. The model was adapted for use with gasoline by updating the fluid properties and recalibrating nondimensional flow coefficients. A detailed surrogate formulation methodology and calculation procedure was used to generate the necessary fluid physical properties for 1-D simulations. Findings from the comparison of the calculated versus measured fuel properties were as follows:

- Calculated properties including density and isobaric specific heat capacity showed good agreement with measurements up to 150°C and 2500 bar.
- Hydraulic model performance was insensitive to changes in other liquid properties, specifically viscosity and thermal conductivity, that were not particularly well captured by the original fuel model.
- Viscosity calculation errors can be significantly reduced by applying generic pressure correlations for liquid hydrocarbons available in the literature.

Even with a good physical property model, however, accurately capturing the hydraulic behavior of gasoline at high

TABLE 9 Genetic search algorithm objective function value versus number of generations.

B50 case runs	Population size	Number of generations	Total number of designs	Objective function value for optimal design
1	16	15	241	8.24
2	16	30	482	8.23
3	16	45	723	8.23
4	16	60	964	8.23

FIGURE 31 Optimal rate shape design solutions versus target profile.

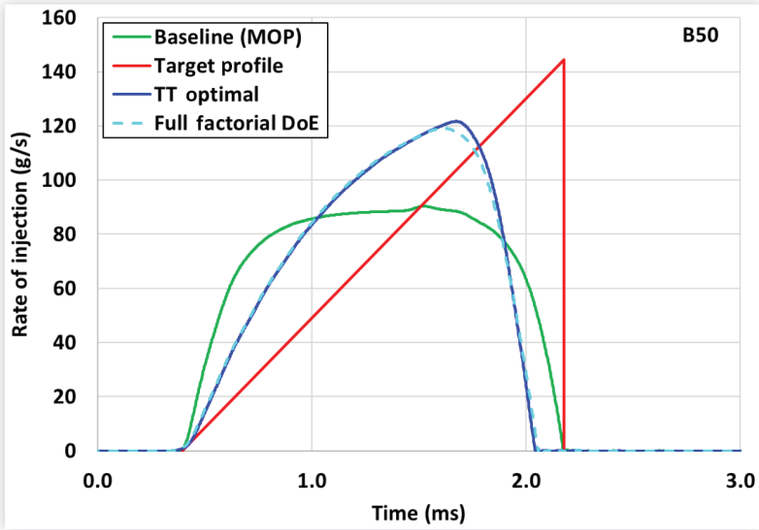

injection pressures required a minor recalibration of all the discharge coefficients. This was achieved by using multi-objective minimization techniques coupled to a genetic search algorithm within GT-SUITE. The major findings from this exercise were as follows:

- Among the different methods investigated, Pareto optimization provided the best closure on the total injected quantity and ROI with measurements.
- It was difficult to reproduce some of the experimentally observed differences in needle dynamics between gasoline and diesel.
- Capturing these effects may require even higher fidelity injector models that include viscous drag or friction effects on moving bodies.

The 1-D gasoline hydraulic model was also used to explore rate shape design for high-pressure GCI applications at a single engine operating point. A triangular fueling profile with a slow opening ramp was targeted as a possible path for demonstrating lower engine-out NOx emissions. Results from a thorough ROI sweep of adjustable hydraulic injector parameters showed that a combination of changes to the nozzle exit hole, needle orifice, and control chamber outlet orifice diameters could be used to approach the desired rate shape. TT is another multi-objective optimization routine available in GT-SUITE and was used to conveniently determine the appropriate set of diameters that most closely matched the triangular ROI. Results from this part of the study are summarized as follows:

- The injector control chamber outlet diameter had to decrease for a slow opening ramp, but the needle orifice and nozzle exit hole diameters had to increase to meet the peak fueling rate constraint.
- A similar combination of diameters and optimal rate shape was achieved using a traditional full-factorial DoE over the same variable search space.
- TT coupled to a genetic search algorithm improved the computational runtime by a factor of 3.6 compared to DoE.

It was beyond the scope of this preliminary study to consider all the adjustable features of the injector for rate shape design. In addition, there are some limitations to the fully flexible rate shaping capability for the baseline hardware and what the 1-D model can explore. For these reasons, it was not possible to exactly match the target profile. Nonetheless, a robust methodology for accurately simulating high-pressure gasoline injection using a 1-D hydraulic model has been demonstrated. A process to determine the optimal set of injector design specifications that generate a desired rate shape with the same model has also been outlined.

TABLE 10 Final injector specifications and computational runtimes after rate shaping.

Method	D_{out} (mm)	D_o (µm)	D_{NO} (mm)	Runtime (hours)
Baseline	0.28	195	1.40	—
TT	0.211	337	2.04	8.4
DoE	0.210	252	2.10	28.3

5. Recommendations

A new rate shape design will ultimately have an impact on the existing combustion system performance and emissions. For this reason, future work will likely focus on coupling the 1-D model to predictive combustion or engine simulations tools.

FIGURE 32 Spray momentum flux for baseline and final rate shape design profiles.

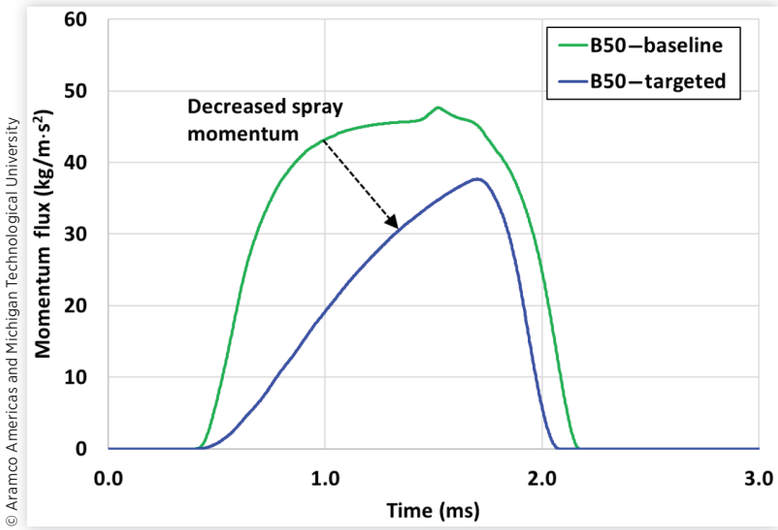

This would provide a means of practical rate shape design using appropriate fuel efficiency, noise, NOx, particulate, and other engine targets for a given GCI application. Hardware that leverages on-demand pressure modulation or needle lift control, such as a direct-acting piezo injector, could also be considered to provide greater flexibility in the fueling profile. Together, all these tools would open an additional pathway to demonstrate even greater performance and emissions benefits for GCI through rate shaping.

Acknowledgment

The 1-D hydraulic model was built by the Fuel Injection System team at IAV GmbH. Needle lift measurements were performed at the 7-BM and 32-ID beamlines at of the APS, Argonne National Laboratory. Usage of the APS was supported by the U.S. DOE under Contract No. DEAC0206CH11357. Liquid fuel property measurements at high temperatures and pressures were conducted at Flucon GmbH.

Contact Information

Tom Tzanetakis
tom.tzanetakis@aramcoamericas.com

Definitions

1-D - One-dimensional
3-D - Three-dimensional
A_o - Total nozzle area (baseline design)
APS - Advanced Photon Source
ASTM - American Society for Testing and Materials
C_c - Contraction coefficient
C_d - Discharge coefficient
$c_{P,l}$ - Isobaric specific heat capacity (liquid)
CFD - Computational fluid dynamics
D_{in} - Control chamber inlet orifice diameter
D_{NO} - Needle orifice diameter
D_o - Nozzle exit hole diameter
D_{out} - Control chamber outlet orifice diameter
D_{sac} - Nozzle sac diameter
DHA - Detailed hydrocarbon analysis
DoE - Design of experiments
E10 - 10% ethanol by volume
EN - European Standard
ET - Solenoid energizing time
f - Objective function
FAME - Fatty acid methyl ester
FBP - Final boiling point
FCM - Flexible control module
GA - Genetic algorithm
GCI - Gasoline compression ignition
HPP - High-pressure pump
HPV - High-pressure relief valve
IA - Injection analyzer
IBP - Initial boiling point
IMV - Inlet metering valve
ISO - International Organization for Standardization
k_l - Thermal conductivity (liquid)
LHV - Lower heating value
m - Constant for viscosity-pressure correlation
m_T - Total injected fuel quantity
$\dot{m}_p$ - Peak mass flow rate

M - Symbol for electric drive motor
MOP - Multi-objective Pareto
MOWS - Multi-objective weighted sum
n - Number of objectives
N - Number of nozzle holes
Nox - Oxides of nitrogen (NO + NO_2)
P - Pressure
P_{sat} - Saturation pressure
Q - Volumetric flow rate
R - Response
RMSE - Root mean square error
ROI - Rate of injection
RON - Research octane number
RPM - Revolutions per minute
RPS - Rail pressure sensor
RVP - Reid vapor pressure
SET - Supplemental emissions test
SOI - Start of injection
t - Time
T - Temperature or symbol for torque flange
TT - Transient targeting
UHC - Unburned hydrocarbons
v - Velocity
W - Response weight factor
WSD - Wear scar diameter
X - Simulation, target or measured value
$\angle$ - Angle
δ - Relative error (% difference)
ΔP - Pressure difference
Δt - Hydraulic injection duration
μ_l - Dynamic viscosity (liquid)
ρ_f - Fuel density
ρ_l - Density (liquid)

References

1. U.S. Energy Information Administration, "Annual Energy Outlook 2021," accessed August 2021, https://www.eia.gov/outlooks/aeo/.
2. International Energy Agency, "World Energy Outlook 2020," accessed August 2021, https://www.iea.org/.
3. Zhang, Y., Voice, A., Tzanetakis, T., Traver, M. et al., "An Evaluation of Combustion and Emissions Performance with Low Cetane Naphtha Fuels in a Multi-Cylinder Heavy-Duty Diesel Engine," *J. Eng. Gas Turb. Power* 138, no. 10 (2016): 102805-1-102805-10, doi:10.1115/1.4032879.
4. Zhang, Y., Sommers, S., Yuanjiang, P., Kumar, P. et al., "Mixing-Controlled Combustion of Conventional and Higher Reactivity Gasolines in a Multi-Cylinder Heavy-Duty Compression Ignition Engine," SAE Technical Paper 2017-01-0696, 2017, doi:https://doi.org/10.4271/2017-01-0696.
5. Lee, J., Zhang, Y., Tzanetakis, T., Traver, M. et al., "Emission Performance of Low Cetane Naphtha as Drop-In Fuel on a Multi-Cylinder Heavy-Duty Diesel Engine and Aftertreatment System," SAE Technical Paper 2017-01-1000, 2017, doi:https://doi.org/10.4271/2017-01-1000.
6. Zhang, Y., Kumar, P., Traver, M., and Cleary, D., "Conventional and Low Temperature Combustion Using Naphtha Fuels in a Multi-Cylinder Heavy-Duty Diesel Engine," *SAE Int. J. Engines* 9, no. 2 (2016): 1021-1035, doi:https://doi.org/10.4271/2016-01-0764.
7. Zhang, Y., Kumar, P., Pei, Y., Traver, M. et al., "An Experimental and Computational Investigation of Gasoline Compression Ignition Using Conventional and Higher Reactivity Gasolines in a Multi-Cylinder Heavy-Duty Diesel Engine," SAE Technical Paper 2018-01-0226, 2017, doi:https://doi.org/10.4271/2018-01-0226.
8. Lee, J., Tzanetakis, T., Zhang, Y., Traver, M. et al., "Characterization of Particulate Matter Emissions from Heavy-Duty Partially Premixed Compression Ignition with Gasoline-Range Fuels," SAE Technical Paper 2019-01-1185, 2017, doi:https://doi.org/10.4271/2019-01-1185.
9. Weber, J., Kakehashi, Y., Hermann, O., Ishihara, A. et al., "Future Heavy-Duty Injection System as Technology Brick for Meeting the 2025 CO_2 Targets," Presented at in *29th Aachen Colloquium on Sustainable Mobility*, Aachen, Germany, October 5-7, 2020.
10. Won, H.-W., Peters, N., Tait, N., and Kalghatgi, G., "Sufficiently Premixed Compression Ignition of a Gasoline-Like Fuel Using Three Different Nozzles in a Diesel Engine," *P. I. Mech. Eng. D-J. Aut.* 226, no. 5 (2012): 698-708, doi:https://doi.org/10.1177/0954407011423453.
11. Won, H.-W., Pitsch, H., Tait, N., and Kalghatgi, G., "Some Effects of Gasoline and Diesel Mixtures on Partially Premixed Combustion and Comparison with the Practical Fuels Gasoline and Diesel in a Compression Ignition Engine," *P. I. Mech. Eng. D-J. Aut.* 226, no. 9 (2012): 1259-1270, doi:https://doi.org/10.1177/0954407012440075.
12. Ciatti, S. and Subramanian, S.N., "An Experimental Investigation of Low-Octane Gasoline in Diesel Engines," *J. Eng. Gas Turb. Power* 133, no. 9 (2011): 092802-1-092802-11, doi:https://doi.org/10.1115/1.4002915.
13. Kolodziej, C.P., Ciatti, S., Vuilleumier, D., Adhidary, B.D. et al., "Extension of the Lower Load Limit of Gasoline Compression Ignition with 87 AKI Gasoline by Injection Timing and Pressure," SAE Technical Paper 2014-01-1302, 2017, doi:https://doi.org/10.4271/2014-01-1302.
14. Sellnau, M., Hoyer, K., Moore, W., Foster, M. et al., "Advancement of GDCI Engine Technology for US 2025 CAFÉ and Tier 3 Emissions," SAE Technical Paper 2018-01-0901, 2017, doi:https://doi.org/10.4271/2018-01-0901.

15. Signorelli, G., Cavani, A., Petrone, M., Petrecchia, S. et al., "GDI Very High Pressure Injector for High Compression Gasoline Engine," Presented at in *42nd International Vienna Motor Symposium*, Vienna, Austria, April 29-30, 2021.
16. Payri, R., Salvador, F.J., Martí-Aldaraví, P., and Martínez-López, J., "Using One-Dimensional Modeling to Analyze the Influence of the Use of Biodiesels on the Dynamic Behavior of Solenoid-Operated Injectors in Common Rail Systems: Detailed Injection System Model," *Energy Convers. Manage.* 54 (2012): 90-99, doi:10.1016/j.enconman.2011.10.004.
17. Salvador, F.J., Gimeno, J., De la Morena, J., and Carreres, M., "Using One-Dimensional Modeling to Analyze the Influence of the Use of Biodiesels on the Dynamic Behavior of Solenoid-Operated Injectors in Common Rail Systems: Results of the Simulations and Discussion," *Energy Convers. Manage.* 54 (2012): 122-132, doi:10.1016/j.enconman.2011.10.007.
18. Kiss, T. and Wolverton, M., "Analytical Comparison of 2- and 3-Way Digital Valves for Use on Direct Needle Control Fuel Injectors," SAE Technical Paper 2004-01-0032, 2017, doi:https://doi.org/10.4271/2004-01-0032.
19. Arcoumanis, C., Gavaises, M., Bostock, P., and Horrocks, R., "Evaluation of Pump Design Parameters in Diesel Fuel Injection Systems," SAE Technical Paper 950078, 2017, doi:https://doi.org/10.4271/950078.
20. Ferrari, A., Pizzo, P., and Paolicelli, F., "Common Feeding Injection System Equipped with Reduced Leakage Solenoid Injectors," SAE Technical Paper 2014-01-2735, 2017, doi:https://doi.org/10.4271/2014-01-2735.
21. Ferrari, A., Pizzo, P., and Vitali, R., "Development and Validation Procedure of a 1D Predictive Model for Simulation of a Common Rail Fuel Injection System Controlled with a Fuel Metering Valve," *SAE Int. J. Engines* 11, no. 4 (2018): 401-422, doi:https://doi.org/10.4271/03-11-04-0027.
22. Tzanetakis, T., Traver, M., Costanzo, V., Medina, R. et al., "Durability Study of a High-Pressure Common Rail Fuel Injection System Using Lubricity Additive Dosed Gasoline-Like Fuel - Additional Cycle Runtime and Teardown Analysis," *SAE Int. J. Adv. & Curr. Prac. In Mobility* 1, no. 2 (2019): 654-674, doi:https://doi.org/10.4271/2019-01-0263.
23. Kolade, B., Morel, T., and Kong, S., "Coupled 1-D/3-D Analysis of Fuel Injection and Diesel Engine Combustion," SAE Technical Paper 2004-01-0928, 2017, doi:https://doi.org/10.4271/2004-01-0928.
24. Sapio, F., Piano, A., Millo, F., and Pesce, F., "Digital Shaping and Optimization of Fuel Injection Pattern for a Common Rail Automotive Diesel Engine through Numerical Simulation," SAE Technical Paper 2017-24-0025, 2017, doi:https://doi.org/10.4271/2017-24-0025.
25. Piano, A., Millo, F., Sapio, F., and Pesce, F., "Multi-Objective Optimization of Fuel Injection Pattern for a Light-Duty Diesel Engine through Numerical Simulation," *SAE Int. J. Engines* 11, no. 6 (2018): 1093-1107, doi:https://doi.org/10.4271/2018-01-1124.
26. Hinkelbein, J., Kremer, F., Lamping, M., Körfer, T. et al., "Experimental Realization of Predefined Diesel Combustion Processes Using Advanced Closed-Loop Combustion Control and Injection Rate Shaping," *Int. J. Engine Res.* 13, no. 6 (2012): 607-615, doi:https://doi.org/10.1177/1468087412439262.
27. Willems, R., Willems, F., Simpson, T., Albrecht, B. et al., "Ramped Versus Square Injection Rate Experiments in a Heavy-Duty Diesel Engine," *SAE Int. J. Adv. & Curr. Prac. In Mobility* 2, no. 3 (2020): 1322-1336, doi:https://doi.org/10.4271/2020-01-0300.
28. Coldren, D., Schuricht, S., and Smith, R., "Hydraulic Electronic Unit Injector with Rate Shaping Capability," SAE Technical Paper 2003-01-1384, 2017, doi:https://doi.org/10.4271/2003-01-1384.
29. Mulemane, A., Han, J., Lu, P., Yoon, S. et al., "Modeling Dynamic Behavior of Diesel Fuel Injection Systems," SAE Technical Paper 2004-01-0536, 2017, doi:https://doi.org/10.4271/2004-01-0536.
30. Dober, G., Tullis, S., Greeves, G., Milovanovic, N. et al., "The Impact of Injection Strategies on Emissions Reduction and Power Output of Future Diesel Engines," SAE Technical Paper 2008-01-0941, 2017, doi:https://doi.org/10.4271/2008-01-0941.
31. Macian, V., Payir, R., Ruiz, S., Bardi, M. et al., "Experimental Study of the Relationship Between Injection Rate Shape and Diesel Ignition Using a Novel Piezo-Actuated Direct-Acting Injector," *Appl. Energy* 118 (2014): 100-113. http://dx.doi.org/10.1016/j.apenergy.2013.12.025.
32. Kohketsu, S., Tanabe, K., and Mori, K., "Flexibly Controlled Injection Rate Shape with Next Generation Common Rail System for Heavy Duty DI Diesel Engines," SAE Technical Paper 2000-01-0705, 2017, doi:https://doi.org/10.4271/2000-01-0705.
33. Tanabe, K., Kohketsu, S., and Nakayama, S., "Effect of Fuel Injection Rate Control on Reduction of Emissions and Fuel Consumption in a Heavy Duty DI Diesel Engine," SAE Technical Paper 2005-01-0907, 2017, doi:https://doi.org/10.4271/2005-01-0907.
34. Naumov, V., Pogulyaev, Y., Baytimerov, R., and Chizhov, D., "New Diesel Engine Fuel Supply System Able to Control Pressure of Pre- and Post-Main Injections," SAE Technical Paper 2015-01-2805, 2017, doi:https://doi.org/10.4271/2015-01-2805.
35. Payri, R., Gimeno, J., De La Morena, J., Battiston, P.A. et al., "Study of New Prototype Pintle Injectors for Diesel Engine Application," *Energy Convers. Manage.* 122 (2016): 419-427. http://dx.doi.org/10.1016/j.enconman.2016.06.003.
36. Rottmann, M., Menne, C., Pischinger, S., Luckhchoura, V. et al., "Injection Rate Shaping Investigations on a Small-Bore DI Diesel Engine," SAE Technical Paper 2009-01-0850, 2017, doi:https://doi.org/10.4271/2009-01-0850.
37. Ferrari, A. and Mittica, A., "Response of Different Injector Typologies to Dwell Time Variations and a Hydraulic Analysis of Closely-Coupled and Continuous Rate Shaping Injection Schedules," *Appl. Energy* 169 (2016): 899-977. http://dx.doi.org/10.1016/j.apenergy.2016.01.120.
38. d'Ambrosio, S. and Ferrari, A., "Exploitation of Injection Fusion Strategies in Diesel Engines Equipped with Solenoid Injectors," *Int. J. Engine Res.* 19, no. 6 (2018): 653-667, doi:https://doi.org/10.1177/1468087417728629.

39. Zhang, T. and Ferrari, A., "Influence of the Injector Setup on Digital and Continuous Injection Rate-Shaping Performance in Diesel Engine Passenger Cars," *Energy Convers. Manage.* 205 (2020): 112259, doi:https://doi.org/10.1016/j.enconman.2019.112259.
40. Zhao, J., Yue, P., Wei, K., and Grekhov, L., "Investigating Effects of Different Influence Factors on the Dynamic Response of a Common-Rail Injector," SAE Technical Paper 2019-01-0272, 2017, doi:https://doi.org/10.4271/2019-01-0272.
41. Mohan, B., Yang, W., and Chou, S.K., "Fuel Injection Strategies for Performance Improvement and Emissions Reduction in Compression Ignition Engines—A Review," *Renew. Sust. Energy Rev.* 28 (2013): 664-676. http://dx.doi.org/10.1016/j.rser.2013.08.051.
42. Boggavarapu, P. and Singh, S., "Computational Study of Injection Rate-Shaping for Emissions Control in Diesel Engines," SAE Technical Paper 2011-26-0081, 2017, doi:https://doi.org/10.4271/2011-26-0081.
43. Yamashita, H., Tomomatsu, K., Toda, N., Shimode, K. et al., "Analysis of Spray to Spray Interaction and Smoke Emission for Diesel Multiple Injections and Quick Rising Injection Rate," SAE Technical Paper 2019-01-2272, 2017, doi:https://doi.org/10.4271/2019-01-2272.
44. Busch, S., Zha, K., Miles, P., Warey, A. et al., "Experimental and Numerical Investigations of Close-Coupled Pilot Injections to Reduce Combustion Noise in a Small-Bore Diesel Engine," *SAE Int. J. Engines* 8, no. 2 (2015): 660-678, doi:https://doi.org/10.4271/2015-01-0796.
45. O'Connor, J. and Musculus, M., "Post Injections for Soot Reduction in Diesel Engines: A Review of Current Understanding," *SAE Int. J. Engines* 6, no. 1 (2013): 400-421, doi:https://doi.org/10.4271/2013-01-0917.
46. Lind, T., Roberts, G., Eagle, W., Rousselle, C. et al., "Mechanisms of Post-Injection Soot-Reduction Revealed by Visible and Diffused Back-Illumination Soot Extinction Imaging," SAE Technical Paper 2018-01-0232, 2017, doi:https://doi.org/10.4271/2018-01-0232.
47. Payri, F., Benajes, J., Pastor, J., and Molina, S., "Influence of the Post-Injection Pattern on Performance, Soot and Nox Emissions in a HD Diesel Engine," SAE Technical Paper 2002-01-0502, 2017, doi:https://doi.org/10.4271/2002-01-0502.
48. Musculus, M. and Kattke, K., "Entrainment Waves in Diesel Jets," *SAE Int. J. Engines* 2, no. 1 (2009): 1170-1193, doi:https://doi.org/10.4271/2009-01-1355.
49. O'Connor, J. and Musculus, M., "Optical Investigation of the Reduction of Unburned Hydrocarbons Using Close-Coupled Post Injections at LTC Conditions in a Heavy-Duty Diesel Engine," *SAE Int. J. Engines* 6, no. 1 (2013): 379-399, doi:https://doi.org/10.4271/2013-01-0910.
50. Knox, B., Genzale, C., Pickett, L., Garcia-Oliver, J. et al., "Combustion Recession after End of Injection in Diesel Sprays," *SAE Int. J. Engines* 8, no. 2 (2015): 679-695, doi:https://doi.org/10.4271/2015-01-0797.
51. Jarrahbashi, D., Kim, S., Knox, B.W., and Genzale, C.L., "Computational Analysis of End-of-Injection Transients and Combustion Recession," *Int. J. Engine Res.* 18, no. 10 (2018): 1088-1110, doi:https://doi.org/10.1177/1468087417701280.
52. Koci, C., Martin, G., Bazyn, T., Morrison, W. et al., "The Influence of Diesel End-of-Injection Rate Shape on Combustion Recession," *SAE Int. J. Engines* 8, no. 2 (2015): 647-659, doi:https://doi.org/10.4271/2015-01-0795.
53. Desantes, J.M., Benajes, J., Molina, S., and González, C.A., "The Modification of the Fuel Injection Rate in Heavy-Duty Diesel Engines. Part 1: Effects on Engine Performance and Emissions," *Appl. Therm. Eng.* 24 (2004): 2701-2714, doi:https//doi.org/10.1016/j.applthermaleng.2004.05.003.
54. Desantes, J.M., Benajes, J., Molina, S., and González, C.A., "The Modification of the Fuel Injection Rate in Heavy-Duty Diesel Engines. Part 2: Effects on Combustion," *Appl. Therm. Eng.* 24 (2004): 2715-2726, doi:https//doi.org/10.1016/j.applthermaleng.2004.05.004.
55. GT-SUITE (v2020, Build 3.0002-Final), computer software, Gamma Technologies LLC., Westmont, IL, 2015.
56. Desantes, J., Salvador, F., Carreres, M., and Jaramillo, D., "Experimental Characterization of the Thermodynamic Properties of Diesel Fuels Over a Wide Range of Pressures and Temperatures," *SAE Int. J. Fuels Lubr.* 8, no. 1 (2015): 190-199, doi:https://doi.org/10.4271/2015-01-0951.
57. Chorazewski, M., Dergal, F., Sawaya, T., Mokbel, I. et al., "Thermophysical Properties of Normafluid (ISO 4113) Over Wide Pressure and Temperature Ranges," *Fuel* 105 (2013): 440-450, doi:https://doi.org/10.1016/j.fuel.2012.05.059.
58. Sarathy, S.M., Farooq, A., and Kalghatgi, G.T., "Recent Progress in Gasoline Surrogate Fuels," *Prog. Energy Combust.* 65 (2018): 67-108, doi:https://doi.org:10.1016/j.pecs.2017.09.004.
59. Tzanetakis, T., Voice, A., and Traver, M., "Accurately Simulating the Performance of Gasoline-Like Fuels in 1-D Hydraulic Injection System Models Operating at High Pressures," SAE Technical Paper 2021-01-0389, 2017, doi:https://doi.org/10.4271/2021-01-0389.
60. European Committee for Standardization, "Automotive Fuels—Diesel—Requirements and Test Methods," EN Standard 590, Revised September 2017.
61. Knothe, G., "A Comprehensive Evaluation of the Cetane Numbers of Fatty Acid Methyl Esters," *Fuel* 119 (2014): 6-13, doi:https://doi.org/10.1016/j.fuel.2013.11.020.
62. Geller, D.P. and Goodrum, J.W., "Effects of Specific Fatty Acid Methyl Esters on Diesel Fuel Lubricity," *Fuel* 83, no. 17 (2004): 2351-2356, doi:https://doi.org/10.1016/j.fuel.2004.06.004.
63. Arkoudeas, P., Karonis, D., Zannikos, F., and Lois, E., "Lubricity Assessment of Gasoline Fuels," *Fuel Process. Technol.* 122 (2014): 107-119, doi:https://doi.org/10.1016/j.fuproc.2014.01.008.
64. Lacey, P. and Mason, R., "Fuel Lubricity: Statistical Analysis of Literature Data," SAE Technical Paper 2000-01-1917, 2017, doi:https://doi.org/10.4271/2000-01-1917.
65. Voice, A., Tzanetakis, T., and Traver, M., "Lubricity of Light-End Fuels with Commercial Diesel Lubricity Additives," SAE Technical Paper 2017-01-0871, 2017, doi:https://doi.org/10.4271/2017-01-0871.

66. Torelli, R., Matusik, K., Nelli, K., Kastengren, A. et al., "Evaluation of Shot-to-Shot In-Nozzle Flow Variations in a Heavy-Duty Diesel Injector Using Real Nozzle Geometry," *SAE Int. J. Fuels Lubr.* 11, no. 4 (2018): 379-295, doi:https://doi.org/10.4271/2018-01-0303.
67. Han, J., Wang, T., Xie, X., Lai, M. et al., "Dynamics of Multiple-Injection Fuel Sprays in a Small-bore HSDI Diesel Engine," SAE Technical Paper 2000-01-1256, 2017, doi:https://doi.org/10.4271/2000-01-1256.
68. Payri, R., Salvador, F.J., Gimeno, J., and Zapta, L.D., "Diesel Nozzle Geometry Influence on Spray Liquid-Phase Fuel Penetration in Evaporative Conditions," *Fuel* 87, no. 7 (2008): 1165-1176, doi:https://doi.org/10.1016/j.fuel.2007.05.058.
69. Som, S., Ramirez, A.I., Longman, D.E., and Aggarwal, S.K., "Effect of Nozzle Orifice Geometry on Spray, Combustion, and Emission Characteristics under Diesel Engine Conditions," *Fuel* 90, no. 3: 1267-1276, doi:https://doi.org/10.1016/j.fuel.2010.10.048.
70. Bower, G. and Foster, D., "A Comparison of the Bosch and Zuech Rate of Injection Meters," SAE Technical Paper 910724, 2017, doi:https://doi.org/10.4271/910724.
71. Shi, J., Guerrassi, N., Dober, G., Karimi, K. et al., "Complex Physics Modelling of Diesel Injector Nozzle Flow and Spray Supported by New Experiments," Presented at in *THIESEL 2014 Conference on Thermo and Fluid Dynamic Processes in Direct Injection Engines*, Valencia, Spain, September 2014.
72. Piano, A., Millo, F., Postrioti, L., Biscontini, G. et al., "Numerical and Experimental Assessment of a Solenoid Common-Rail Injector Operation with Advanced Injection Strategies," *SAE Int. J. Engines* 9, no. 1 (2016): 565-575, doi:https://doi.org/10.4271/2016-01-0563.
73. Piano, A., Boccardo, G., Millo, F., Cavicchi, A. et al., "Experimental and Numerical Assessment of Multi-Event Injection Strategies in a Solenoid Common-Rail Injector," *SAE Int. J. Engines* 10, no. 4 (2017): 2129-2140, doi:https://doi.org/10.4271/2017-24-0012.
74. Aspen, H.Y.S.Y.S., computer software, Aspen Technology Inc., Bedford, MA, 1994.
75. Voice, A.K. and Tzanetakis, T., Method to generate accurate thermodynamic and physical fluid properties of real light-distillate fuels for one-dimensional hydraulic models using a detailed multi-component surrogate formulation approach. U.S. Patent Application No. 17/036,359, filed September 29, 2020.
76. Bode, B., "Bedeutung der Dichte für Transportgrößen von Flüssigkeiten unter hohem Druck," *Erdöl Erdgas Kohle (in German)* 107 (1991): 228, 231.
77. Kashiwagi, H. and Makita, T., "Viscosity of Twelve Hydrocarbon Liquids in the Temperature Range 298-348 K at Pressures up to 110 Mpa," *Int. J. Thermophys.* 3, no. 4 (1982): 289-305, doi:https://doi.org/10.1007/BF00502346.
78. Bode, B., "Entwicklung eines Quarzviskosimeters für Messungen bei hohen Drücken," Dissertation (in German), Technical University of Clausthal, 1984.
79. Bode, B., "Entwicklung eines Quarzviskosimeters für Messungen bei hohen Drücken," *Tribologie und Schmierungstechnik (in German)* 35, no. 5 (1988): 256-261.
80. Diller, D.E. and Frederick, N.V., "Torsional Piezoelectric Crystal Viscometer for Compressed Gases and Liquids," *Int. J. Thermophys.* 10, no. 1 (1989): 145-157, doi:https://doi.org/10.1007/BF00500715.
81. Wakeham, W.A. and Richardson, S.M., "The Torsional Quartz-Crystal Viscometer," *Int. J. Thermophys.* 42 (2021): 120-160, doi:https://doi.org/10.1007/s10765-021-02807-y.
82. Bode, B., "Messung der Wärmeleitfähigkeit von Flüssigkeiten unter hohem Druck," *Erdöl Erdgas Kohle (in German)* 107 (1991): 77-80.
83. Mylona, S.K., Yang, X., Hughes, T.J., White, A.C. et al., "High-Pressure Thermal Conductivity Measurements of a (Methane + Propane) Mixture with a Transient Hot-Wire Apparatus," *J. Chem. Eng. Data* 65, no. 2 (2020): 906-915, doi:https://doi.org/10.1021/acs.jced.9b01087.
84. American Society for Testing and Materials, "Standard Test Method for Thermal Conductivity, Thermal Diffusivity, and Volumetric Heat Capacity of Engine Coolants and Related Fluids by Transient Hot Wire Liquid Thermal Conductivity Method," ASTM Standard D7896, Revised 2019.
85. American Society for Testing and Materials, "Standard Test Method for Specific Heat of Liquids and Solids," ASTM Standard D2766, Revised 2009.
86. Gunantara, N., "A Review of Multi-Objective Optimization: Methods and Its Applications," *Cogent Engineering* 5 (2018): 1, doi:https://doi.org/10.1080/23311916.2018.1502242.
87. Gamma Technologies LLC., "GT-SUITE Optimization Manual," Version 2021, Westmont, IL, 2020, 38-40.
88. Tamaki, H., Kita, H., and Kobayashi, S., "Multi-Objective Optimization by Genetic Algorithms: A Review," in *Proceedings of IEEE International Conference on Evolutionary Computation*, Nagoya, Japan, 1996, 517-522, https://doi.org/10.1109/ICEC.1996.54265.
89. Lin, C.D., Anderson-Cook, C.M., Hamada, M.S., Moore, L.M. et al., "Using Genetic Algorithms to Design Experiments: A Review," *Qual. Reliab. Eng. Int.* 31, no. 2 (2015): 155-167, doi:https://doi.org/10.1002/qre.1591.
90. Atashkari, K., Nariman-Zadeh, N., Pilechi, A., Jamali, A. et al., "Thermodynamic Pareto Optimization of Turbojet Engines Using Multi-Objective Genetic Algorithms," *Int. J. Therm. Sci.* 44, no. 11 (2005): 1061-1071, doi:https://doi.org/10.1016/j.ijthermalsci.2005.03.016.
91. Moiz, A., Pal, P., Probst, D., Pei, Y. et al., "A Machine Learning-Genetic Algorithm (ML-GA) Approach for Rapid Optimization Using High-Performance Computing," *SAE Int. J. Commer. Veh.* 11, no. 5 (2018): 291-306, doi:https://doi.org/10.4271/2018-01-0190.
92. Deb, K. and Jain, H., "An Evolutionary Many-Objective Optimization Algorithm Using Reference-Point-Based Nondominated Sorting Approach, Part I: Solving Problems with Box Constraints," *IEEE Transactions on Evolutionary Computation* 18, no. 4 (2014): 577-601, doi:https://doi.org/10.1109/TEVC.2013.2281535.
93. Orbey, H. and Sandler, S.I., "The Prediction of the Viscosity of Liquid Hydrocarbons and their Mixtures as a Function of

Temperature and Pressure," *Can. J. Chem. Eng.* 71, no. 3 (1993): 437-446, doi:https://doi.org/10.1002/cjce.5450710314.

94. Yasutomi, K., Hwang, J., Manin, J., Pickett, L. et al., "Diesel Injector Elasticity Effects on Internal Nozzle Flow," SAE Technical Paper 2019-01-2279, 2017, doi:https://doi.org/10.4271/2019-01-2279.
95. Torelli, R., Sforzo, B.A., Matusik, K.E., Kastegren, A.L. et al., "Investigation of Shot-to-Shot Variability during Short Injections," Presented at in *14th Triennial International Conference on Liquid Atomization and Sprays Systems (ICLASS 2018)*, Chicago, IL, July 22-26, 2018.
96. Torelli, R., Matusik, K.E., Sforzo, B.A., Kastengren, A. et al., "In-Nozzle Cavitation-Induced Orifice-to Orifice Variations Using Real Injection Geometry and Gasoline-Like Fuels," Presented at in *10th International Symposium on Cavitation (CAV2018)*, Baltimore, MD, May 14-16, 2018.
97. Torelli, R., Magnotti, G., Som, S., Pei, Y. et al., "Exploration of Cavitation-Suppressing Orifice Designs for a Heavy-Duty Diesel Injector Operating with Straight-Run Gasoline," SAE Technical Paper 2019-24-0126, 2017, doi:https://doi.org/10.4271/2019-24-0126.
98. Torelli, R., Pei, Y., Zhang, Y., Traver, M. et al., "Effect of Fuel Temperature on the Performance of a Heavy-Duty Diesel Injector Operating with Gasoline," SAE Technical Paper 2021-01-0547, 2017, doi:https://doi.org/10.4271/2021-01-0547.
99. Kocher, L. "Final Scientific/Technical Report: Enabling Technologies for Heavy-Duty Vehicles—Cummins 55BTE," Cummins Inc., Columbus, IN, 168, September 29, 2018, https://doi.org/10.2172/1474075.

Appendix A

TABLE A.1 Measured RON60 gasoline fuel properties at high pressures and temperatures.

T (°C)	P (bar, gauge)	μ_l (mPa·s)	ρ_l(kg/m^3)	$c_{P,l}$ (kJ/kg·K)	K (W/m·K)
–20	0	0.6651	742.5	1.928	0.1276
–20	200	0.7815	755.9	1.901	0.1312
–20	500	1.034	774.0	1.884	0.1353
–20	1000	1.479	797.9	1.875	0.1413
–20	1500	2.193	818.6	1.874	0.1463
–20	2500	4.980	850.6	1.875	0.1542
20	0	0.4230	708.3	2.135	0.1146
20	200	0.5196	726.0	2.098	0.1190
20	500	0.6624	747.6	2.082	0.1240
20	1000	0.9750	775.5	2.082	0.1313
20	1500	1.435	798.8	2.084	0.1368
20	2500	3.102	835.0	2.091	0.1456
80	0	—	—	—	—
80	200	0.3196	683.2	2.361	0.1038
80	500	0.4182	712.3	2.363	0.1110
80	1000	0.6166	747.5	2.375	0.1197
80	1500	0.9350	775.2	2.383	0.1263
80	2500	1.846	816.7	2.397	0.1369
120	0	—	—	—	—
120	200	0.2673	657.4	2.556	0.0961
120	500	0.3496	692.9	2.571	0.1049
120	1000	0.5106	733.7	2.587	0.1150
120	1500	0.7546	764.6	2.598	0.1225
120	2500	1.522	810.7	2.607	0.1338
150	0	—	—	—	—
150	200	0.2320	640.6	2.715	0.0917
150	500	0.3157	681.3	2.736	0.1019
150	1000	0.4737	726.9	2.750	0.1129
150	1500	0.7083	760.7	2.757	0.1213
150	2500	1.474	809.7	2.757	0.1334

TABLE A.2 Generated RON60 gasoline fuel properties using the methodology in Section 2.6 and Aspen HYSYS.

T (°C)	P (bar, gauge)	μ_l (mPa·s)	ρ_l(kg/m^3)	$c_{P,l}$ (kJ/kg·K)	K (W/m·K)
−20	0	0.6895	740.8	1.865	0.1295
−20	200	0.6993	755.5	1.837	0.1295
−20	500	0.7114	774.0	1.814	0.1295
−20	1000	0.7271	798.6	1.794	0.1295
−20	1500	0.7395	818.4	1.783	0.1295
−20	2500	0.7584	849.2	1.771	0.1295
20	0	0.4141	705.6	2.072	0.1189
20	200	0.4220	724	2.030	0.1189
20	500	0.4312	746.1	1.999	0.1189
20	1000	0.4425	774.2	1.974	0.1189
20	1500	0.4511	795.9	1.961	0.1189
20	2500	0.4638	828.9	1.948	0.1189
80	0	—	—	—	—
80	200	0.2373	676.5	2.308	0.1024
80	500	0.2448	706.2	2.262	0.1024
80	1000	0.2531	740.7	2.230	0.1024
80	1500	0.2590	765.7	2.216	0.1024
80	2500	0.2673	802	2.201	0.1024
120	0	—	—	—	—
120	200	0.1729	643.7	2.486	0.0901
120	500	0.1798	679.7	2.426	0.0901
120	1000	0.1869	718.3	2.391	0.0901
120	1500	0.1917	745.2	2.375	0.0901
120	2500	0.1983	783.2	2.361	0.0901
150	0	—	—	—	—
150	200	0.1387	618.8	2.615	0.0775
150	500	0.1454	660.4	2.544	0.0775
150	1000	0.1517	702.3	2.506	0.0775
150	1500	0.1558	730.5	2.490	0.0775
150	2500	0.1614	769.5	2.475	0.0775

TABLE A.3 Recalculated dynamic viscosity of RON60 gasoline using the correlation in Equation 5 [93].

T (°C)	P (bar, gauge)	μ_l (mPa·s)
−20	0	0.6917
−20	200	0.8415
−20	500	1.1291
−20	1000	1.8430
−20	1500	3.0083
−20	2500	8.0155
20	0	0.4152
20	200	0.5051
20	500	0.6778
20	1000	1.1064
20	1500	1.8060
20	2500	4.8119
80	0	—
80	200	0.2803
80	500	0.3761
80	1000	0.6139
80	1500	1.0021
80	2500	2.6701
120	0	—
120	200	0.2010
120	500	0.2697
120	1000	0.4403
120	1500	0.7187
120	2500	1.9150
150	0	—
150	200	0.1581
150	500	0.2121
150	1000	0.3463
150	1500	0.5652
150	2500	1.5061